The Journal of Physiology

Computational analysis of the human sinus node action potential: model development and effects of mutations

Alan Fabbri[1], Matteo Fantini[1], Ronald Wilders[2] and Stefano Severi[1]

[1] *Computational Physiopathology Unit, Department of Electrical, Electronic and Information Engineering "Guglielmo Marconi", University of Bologna, Cesena, Italy*
[2] *Department of Anatomy, Embryology and Physiology, Academic Medical Center, University of Amsterdam, Amsterdam, The Netherlands*

Key points

- We constructed a comprehensive mathematical model of the spontaneous electrical activity of a human sinoatrial node (SAN) pacemaker cell, starting from the recent Severi–DiFrancesco model of rabbit SAN cells.
- Our model is based on electrophysiological data from isolated human SAN pacemaker cells and closely matches the action potentials and calcium transient that were recorded experimentally.
- Simulated ion channelopathies explain the clinically observed changes in heart rate in corresponding mutation carriers, providing an independent qualitative validation of the model.
- The model shows that the modulatory role of the 'funny current' (I_f) in the pacing rate of human SAN pacemaker cells is highly similar to that of rabbit SAN cells, despite its considerably lower amplitude.
- The model may prove useful in the design of experiments and the development of heart-rate modulating drugs.

Abstract The sinoatrial node (SAN) is the normal pacemaker of the mammalian heart. Over several decades, a large amount of data on the ionic mechanisms underlying the spontaneous electrical activity of SAN pacemaker cells has been obtained, mostly in experiments on single cells isolated from rabbit SAN. This wealth of data has allowed the development of mathematical models of the electrical activity of rabbit SAN pacemaker cells. The present study aimed to construct a comprehensive model of the electrical activity of a human SAN pacemaker cell using recently obtained electrophysiological data from human SAN pacemaker cells. We based our model on the recent Severi–DiFrancesco model of a rabbit SAN pacemaker cell. The action potential and calcium transient of the resulting model are close to the experimentally recorded values. The model has a much smaller 'funny current' (I_f) than do rabbit cells, although its modulatory role is highly similar. Changes in pacing rate upon the implementation of mutations associated with sinus node dysfunction agree with the clinical observations. This agreement holds for both loss-of-function and gain-of-function mutations in the *HCN4*, *SCN5A* and *KCNQ1* genes, underlying ion channelopathies in I_f, fast sodium current and slow delayed rectifier potassium current, respectively. We conclude that our human SAN cell model can be a useful tool in the design of experiments and the development of drugs that aim to modulate heart rate.

(Resubmitted 24 December 2016; accepted after revision 2 February 2017; first published online 9 February 2017)
Corresponding author S. Severi: Department of Electrical, Electronic and Information Engineering 'Guglielmo Marconi', University of Bologna, Via Venezia 52, 47521 Cesena (FC), Italy. Email: stefano.severi@unibo.it

 DOI: 10.1113/JP273259

Abbreviations AP, action potential; APA, action potential amplitude; APD_{20}, APD_{50} and APD_{90}, action potential duration at 20%, 50% and 90% of repolarization; Ca_i range, diastolic–systolic range of intracellular free calcium concentration; CaT, calcium transient; CL, cycle length; DD, diastolic depolarization; DDR_{100}, diastolic depolarization rate over the first 100 ms of diastolic depolarization; $(dV/dt)_{max}$, maximum rate of rise of membrane potential; *HCN4*, hyperpolarization-activated cyclic nucleotide-gated cation channel 4; Iso, isoprenaline; *KCNQ1*, potassium voltage-gated channel subfamily Q member 1; MDP, maximum diastolic potential; OS, overshoot; RyR, ryanodine receptor; SAN, sinoatrial node; *SCN5A*, sodium voltage-gated channel α subunit 5; SERCA, sarco-endoplasmic reticulum Ca^{2+}-ATPase; TA, intracellular CaT amplitude; TD_{20}, TD_{50} and TD_{90}, intracellular CaT duration at 20%, 50% and 90% of calcium decay.

Introduction

There is no need to explain the important role of the sinoatrial node (SAN) in cardiac function. Many studies have focused on this small but crucial piece of cardiac tissue and provided detailed knowledge of the physiological processes governing its function. Yet we still have an incomplete understanding of the cellular basis of the pacemaker activity of the SAN and, specifically, the degree of contribution of the different mechanisms involved is still debated (Lakatta & DiFrancesco, 2009; DiFrancesco, 2010; Lakatta, 2010; Maltsev & Lakatta, 2010; Noble *et al.* 2010; Verkerk & Wilders, 2010; Himeno *et al.* 2011; DiFrancesco & Noble, 2012; Lakatta & Maltsev, 2012; Rosen *et al.* 2012; Monfredi *et al.* 2013; Yaniv *et al.* 2013, 2015).

To date, almost all experiments on SAN electrophysiology have been carried out on animals, particularly rabbits. These experiments have shed light on several aspects, such as characteristics of membrane currents, effects of ion channel blockers, calcium handling and beating rate modulation. This considerable amount of data has allowed the development of increasingly comprehensive and detailed action potential (AP) models (Wilders, 2007) subsequent to the first mathematical models reproducing pacemaker activity being created (McAllister *et al.* 1975; Yanagihara *et al.* 1980; Noble & Noble, 1984; DiFrancesco & Noble, 1985). Recently, novel SAN AP models have been proposed, incorporating detailed calcium-handling dynamics and providing in-depth descriptions of the underlying events at the cellular level in guinea-pig, mouse and rabbit (Himeno *et al.* 2008; Maltsev & Lakatta, 2009; Kharche *et al.* 2011; Severi *et al.* 2012).

However, the translation of animal data/models to humans is not straightforward (probably even less so for SAN pacemaker cells than working myocardial cells), given the big difference in their main 'output' (i.e. pacing rate) between human and laboratory animals.

Very few measurements are available for human SAN cells because failing explanted hearts, as obtained during heart transplantation, usually do not contain the SAN region, which remains inside the receiver's chest. Drouin (1997) was the first to record human adult APs from SAN tissue, obtained from four subjects affected by left ventricle infarction. Ten years later, Verkerk *et al.* (2007*b*) investigated the electrophysiological properties of three isolated SAN cells from a woman who underwent SAN excision because of a paroxysmal non-treatable tachycardia. They recorded APs and characterized the funny current using whole-cell patch clamp in current clamp and voltage clamp mode. In a subsequent study (Verkerk *et al.* 2013), the same group reported further data from the same patient, regarding the calcium transient (CaT) measured by indo-1 fluorescent dye.

Some proof-of-concept attempts have been made to model spontaneous activity in human cardiac pacemaker cells. Seemann *et al.* (2006) presented the first human SAN AP model as part of a wider 3D model of human atria. Their model started from the model of Courtemanche *et al.* (1998) of the human atrial AP and achieved automaticity by including rabbit SAN currents (e.g. I_f, I_{CaT}, etc.), formulated in accordance with Zhang *et al.* (2000). Unfortunately, no reliable experimental comparisons could be made with the model of Seemann *et al.* (2006). Chandler *et al.* (2009) described the 'molecular architecture' of adult human SAN tissue obtained from healthy hearts, comparing it to the non-specialized tissue of the right atrium. They developed a SAN model, again starting from the model of Courtemanche *et al.* (1998); by scaling the maximal conductances based on mRNA data, they provided a proof of concept that automaticity can be the result of the specific gene expression pattern of human SAN tissue. However, some mechanisms were not included, and no quantitative AP features were computed or compared with the human data available at that time. Accordingly, as Chandler *et al.* (2009) themselves affirmed, 'the resulting model cannot be considered definitive and is a guide only'.

Recently, Verkerk and Wilders (2015) computationally investigated mutations affecting hyperpolarization-activated cyclic nucleotide-gated cation channel 4 (*HCN4*) channels, but they '. . . preferred to study I_f in simulated action potential clamp experiments, thus ensuring that the action potential followed the course of that of a human SAN pacemaker cell' because a human SAN AP model was not formulated yet. Thus, they highlighted the need for such a model.

Much more recent is the human SAN AP model formulated by Pohl *et al.* (2016). In their model, to

investigate the cardiac neuromodulation (as exerted by vagal stimulation) that aims to reduce heart rate, they focused their attention on the effects that ACh has on the rate. Starting from the rabbit SAN model reported by Dokos *et al.* (1996), they updated current formulations, integrating data from human SAN cells (Verkerk *et al.* 2007*b*) and human ion channels expressed in heterologous systems (HEK or tsA-201 cells, *Xenopus* oocytes, etc.). The simulated cycle length (CL) was in accordance with the experimental recordings of human SAN cell APs by Verkerk *et al.* (2007*b*) but, unfortunately, the AP morphology, both during the diastolic depolarization (DD) phase and AP, was very unlike that obtained experimentally.

The main aim of the present study is the formulation of a human SAN AP model strictly based on and constrained by the available electrophysiological data. We started from the recent rabbit SAN model by Severi *et al.* (2012), which integrates the two principal mechanisms that determine the beating rate: the 'membrane clock' and 'calcium clock' (Maltsev & Lakatta, 2009; Lakatta *et al.* 2010). Several current formulations were updated based on available measurements. A set of parameters, for which no specific data were available, were tuned to reproduce the measured AP and calcium transient data. We then used the model to assess the effects of several mutations affecting heart rate and investigated the rate modulation in some relevant conditions.

Methods

Model development

The starting point of our work was the rabbit SAN cell model by Severi *et al.* (2012). Several currents, pumps and exchangers were reviewed, based on electrophysiological data from human SAN cells (Verkerk *et al.* 2007*b*), self-beating embryonic human cardiomyocytes (Danielsson *et al.* 2013), as selected for their automaticity, and data on gene expression patterns in SAN *vs.* atrial human cells (Chandler *et al.* 2009). Specifically, the model was constrained by: AP parameters obtained from three isolated human SAN pacemaker cells by Verkerk *et al.* (2007*b*); the voltage clamp data on I_f in the same three cells (Verkerk *et al.* 2007*b*); the effect of 2 mM Cs^+, as an I_f blocker, on the AP of a single isolated human SAN pacemaker cell (Verkerk *et al.* 2007*b*); and the Ca^{2+} transient data of a single isolated human SAN pacemaker cell (Verkerk *et al.* 2013). For a small set of parameters for which no specific experimental data were available, values were obtained via an automatic optimization procedure (see below).

Figure 1 shows a schematic diagram of the human SAN AP model. The compartmentalization, essential for the calcium handling description, is inherited from the parent model, as were the sarcolemmal ionic currents, pumps and exchangers. The ultrarapid delayed rectifier K^+ current (I_{Kur}) was developed independently. Table 1 reports the changes with respect to the rabbit SAN model and the rationale for each. All model equations and parameter values are provided in Appendix 1.

Automatic optimization procedure

An automatic optimization was performed to tune the parameters for which human experimental data were not available to fit the recorded AP and cytosolic calcium transient traces (Verkerk *et al.* 2007*b*, 2013).

The cost function of the optimization procedure was based on quantitative data on AP features [action potential amplitude (APA), maximum diastolic potential (MDP), CL, maximum rate of rise of membrane potential [$(dV/dt)_{max}$], action potential duration (APD_{20}, APD_{50}, APD_{90}), diastolic depolarization rate (DDR_{100})], intracellular calcium transients [diastolic $[Ca^{2+}]_i$, systolic $[Ca^{2+}]_i$, intracellular CaT duration (TD_{20}, TD_{50}, TD_{90})] and the effect of the administration of 2 mM Cs^+, a funny current blocker, on CL (Verkerk *et al.* 2007*b*, 2013). The most critical features (CL, MDP and CL prolongation in response to Cs^+) were weighted more heavily.

After each simulation, the set of quantitative descriptors was extracted and compared with the experimental data.

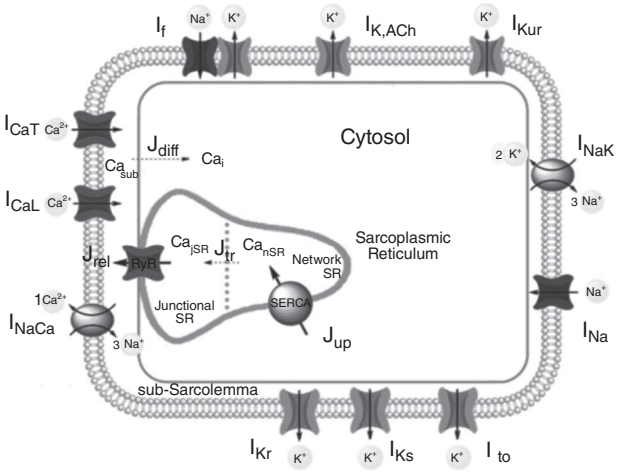

Figure 1. Schematic diagram of the human SAN cell model
The cell is divided into three compartments: subsarcolemma, cytosol and sarcoplasmic reticulum (SR), which is subdivided into junctional and network SR. Ca^{2+} handling is described by: two diffusion fluxes (J_{diff} from the subsarcolemmal space to the cytosol and J_{tr} from the network SR to the junctional SR), the Ca^{2+} uptake from the cytosol into the network SR by the SERCA pump (J_{up}) and the Ca^{2+} release (J_{rel}) from the junctional SR into the subsarcolemmal space by the RyRs. Sodium, calcium and potassium ions pass the sarcolemmal membrane through 11 different ionic channels, pumps and exchangers, as indicated.

Table 1. Changes in human SAN cell model with respect to the parent model

	Update	Rationale
Cell capacitance and dimensions	$C_m = 57$ pF, $L_{cell} = 67$ μm, $R_{cell} = 3.9$ μm	Human SAN data (Verkerk *et al*. 2007*b*)
I_f	New formulation	Human SAN data (Verkerk *et al*. 2007*b*)
I_{Kr}	New steady-state activation, $g_{Kr} = +10\%$	Embryonic human data (Danielsson *et al*. 2013)
I_{Ks}	New steady-state activation, $g_{Ks} = -78\%$	Embryonic human data (Danielsson *et al*. 2013)
I_{Kur}	Added, $g_{Kur} = 6\%$ of atrial formulation from Maleckar *et al*. (2009) atrial cell model	Gene expression data (Chandler *et al*. 2009) and automatic optimization (APD)
I_{to}	$g_{to} = -1.5\%$	Automatic optimization (OS)
$I_{K,ACh}$	$g_{K,ACh} = -77.5\%$	Fitting of ACh effects in rabbit
I_{NaK}	$I_{NaK,max} = -28\%$	Automatic optimization (CL)
I_{CaL}	$V_{½,dL} = -16.45$ mV, $k_{dL} = 4.337$ mV (dL gate) $P_{CaL} = +28.5\%$	Automatic optimization (CL)
I_{CaT}	$P_{CaT} = +15\%$	Automatic optimization (early DD)
I_{NaCa}	$K_{NaCa} = -53\%$	Automatic optimization (diastolic $[Ca^{2+}]_i$)
SR uptake (J_{up})	Sigmoidal formulation	Fitting of diastolic $[Ca^{2+}]_i$
SR release (J_{rel})	$k_s = 1.48 \times 10^8$ s^{-1} $k_{om} = 660$ s^{-1}	Automatic optimization (Ca_i range)
Calmodulin	$kf_{CM} = 1.64 \times 10^6$ (mM s)$^{-1}$	Automatic optimization (Ca_i range)
Calsequestrin	$kf_{CQ} = 175.4$ (mM s)$^{-1}$	Automatic optimization (Ca_i range)
Calcium diffusion	$\tau_{difCa} = 5.469 \times 10^{-5}$ s	Automatic optimization (Ca_i range)
Intracellular Na	Fixed at 5 mM	As used in human SAN experiments (Verkerk *et al*. 2007*b*)

C_m, membrane capacitance; L_{cell}, R_{cell}, length and radius of the cell; g_i, maximal conductance for the *i* type channel; $I_{NaK,max}$ = maximal activity of Na^+/K^+ pump; P_{CaT}, P_{CaL}, permeability for the T- and L-type calcium currents; $V_{½,dL}$, k_{dL}, half-activation potential and slope factor for voltage-dependent *dL* gate; K_{NaCa}, maximal current of NCX; k_s, Ca^{2+} diffusion rate for RyR channels; k_{om}, RyR deactivation rate; kf_{CM}, kf_{CQ}, association constants for calmodulin and calsequestrin. The reported features in parentheses (APD, CL, Ca_i range, DD, OS) are those that were most impacted during the automatic optimization procedure.

If a particular observed feature fell out of the experimental mean ± SEM range, the contribution of this feature to the overall cost was increased in a linear way; otherwise, no handicap was added. The search for the optimal solution was conducted using the Nelder–Mead simplex method (Lagarias *et al.* 1998). The obtained parameters are shown in Table 1. Further details on the optimization procedure are reported in Appendix 2.

Cell capacitance and dimensions

We assumed a membrane capacitance (C_m) of 57 pF, and a cylindrical cell shape with a length of 67 μm and a diameter of 7.8 μm, in accordance with the experimental data of Verkerk *et al.* (2007*b*), who reported values of 56.6 ± 8.7 pF, 66.7 ± 6.3 μm and 7.8 ± 0.4 μm (mean ± SEM, $n = 4$), respectively. The dimensions of the intracellular compartments, expressed as a percentage of cell volume, were adopted from the parent model.

Membrane currents

Here, we specify each of the sarcolemmal currents flowing through the ionic channels, pumps and exchangers shown in Fig. 1, except for $I_{K,ACh}$, which is described in the section 'Autonomic modulation'. All membrane currents were scaled up by the new value of the cell capacitance, aiming to maintain the conductance densities adopted from the parent model. Changes to the conductance densities, as a result of parameter tuning, are reported in the corresponding current subsections.

Funny current (I_f). From their experiments on human SAN cells, Verkerk *et al.* (2007*b*) reported a maximal I_f conductance of 75.2 ± 3.8 pS/pF (mean ± SEM, $n = 3$). Consequently, we assumed a maximal I_f conductance (g_f) of 4.3 nS, given our C_m of 57 pF. The funny current was implemented by splitting it into Na^+ and K^+ components, with a $\frac{g_{fNa}}{g_{fK}}$ conductance ratio of 0.5927, thus arriving at an I_f reversal potential (E_f) of –22 mV, in accordance with the experimentally determined value of –22.1 ± 2.4 mV (mean ± SEM, $n = 3$) (Verkerk *et al.* 2007*b*). A first-order Hodgkin and Huxley-type kinetic scheme was assumed for I_f activation, as described by the formulations presented by Verkerk *et al.* (2007*a*) and Verkerk and Wilders (2010). The activation time constant τ_y was formulated in accordance with Verkerk *et al.* (2007*a*), who used a Dokos

et al. (1996)-type equation to fit the experimental data obtained from three human adult SAN cells by Verkerk *et al.* (2007*b*).

Rapid delayed rectifier K^+ current (I_{Kr}). The steady-state activation curve of I_{Kr} (*pa* gate) was fitted to data from embryonic human cardiomyocytes by Danielsson *et al.* (2013). The measured tail current density following activation pulses from −70 to +50 mV was normalized with respect to the maximal measured value and then fitted with a Boltzmann equation. The conductance g_{Kr} was set to 4.2 nS (+10% compared to parent model) to hyperpolarize the maximum diastolic potential (MDP) and obtain the value experimentally observed in human SAN (Drouin, 1997; Verkerk *et al.* 2007*b*).

Slow delayed rectifier K^+ current (I_{Ks}). The steady-state activation curve for I_{Ks} (*n* gate) was updated in accordance with the experimental data of Danielsson *et al.* (2013). The reported current density *vs.* voltage data were normalized to the maximal measured value and subjected to square-root, in line with the second-order Hodgkin and Huxley-type kinetic scheme. Data were then fitted with a Boltzmann equation. The conductance g_{Ks} was set to 0.65 nS (11.4 pS/pF), −78% with respect to the parent model, as a result of the automatic optimization procedure. On one hand, Chandler *et al.* (2009) reported an mRNA expression level in the human SAN equal to 69% of that in non-specialized atrium cells. On the other hand, very discordant values have been reported for g_{Ks} in human atrial cells up to now, ranging from 3.5 pS/pF (Grandi *et al.* 2011) to 20 pS/pF (Nygren *et al.* 1998), whereas g_{Ks} was adjusted to 129 pS/pF in the model of Courtemanche *et al.* (1998) simply to match AP duration.

Ultrarapid delayed rectifier K^+ current (I_{Kur}). Chandler *et al.* (2009) reported the expression of $K_V1.5$ channels, responsible for I_{Kur}, in human SAN tissue. Because I_{Kur} was not present in the parent model, we added this current, formulating it as in the human atrial cell model of Maleckar *et al.* (2009). The g_{Kur} conductance was set to 0.1539 nS, 6% of the corresponding atrial value, based on the automatic optimization procedure.

Transient outward K^+ current (I_{to}). We maintained the parent model formulation, which, in turn, was adopted from the model of Maltsev & Lakatta (2009). The conductance g_{to} was set to 3.5 nS, slightly reduced (−1.5%) compared to the rabbit SAN model.

Sodium/potassium pump current (I_{NaK}). The formulation by Severi *et al.* (2012), which was in turn derived from that of Kurata *et al.* (2002), was adopted. The maximal activity of the Na^+/K^+ pump was reduced by 28% ($I_{NaK,max} = 0.08105$ nA) through automatic optimization.

Sodium current (I_{Na}). The presence of fast Na^+ current (I_{Na}) in human SAN cells has been reported by Verkerk *et al.* (2009*b*). The steady-state activation and inactivation curves (gates *m* and *h*) of the parent model have been simply rewritten in a sigmoidal formulation (see Appendix 1) to facilitate the implementation of mutations related to $Na_v1.5$ channels.

T-type Ca^{2+} current (I_{CaT}). The mathematical formulation of I_{CaT} was inherited from the parent model and thus based on the constant field equation by Sarai *et al.* (2003). The Ca^{2+} permeability P_{CaT} was set to 0.04132 nA mM^{-1} (+15%), as obtained by automatic optimization.

L-type Ca^{2+} current (I_{CaL}). Changes in I_{CaL} kinetics were limited to the voltage-dependent steady-state activation curve dL_∞. The half-maximal activation voltage ($V_{½,dL}$) was slightly shifted towards less negative potentials (from −20.3 to −16.45 mV) and the slope factor k_{dL} was slightly increased (from 4.2 to 4.337 mV). The Ca^{2+} permeability was increased by 28% (P_{CaL} = 0.4578 nA mM^{-1}). All of these parameters were updated using automatic optimization.

Sodium/calcium exchange current (I_{NaCa}). The set of equations describing the Na^+/Ca^{2+} exchanger activity was adopted from the parent model and thus originally derived by Kurata *et al.* (2002). The maximal current provided by the exchanger was set to 3.343 nA, reduced by 53% as a result of the automatic optimization procedure.

Calcium handling

As in the parent model, the mathematical formulation of Ca^{2+} handling was based on Maltsev and Lakatta (2009), who provided an advanced description of SR behaviour. The parameter updates, which play an important role in Ca^{2+} handling, were achieved by automatic optimization.

SR Ca^{2+} uptake (J_{up}). The Ca^{2+} uptake flux was formulated by a sigmoidal curve, instead of the Michaelis–Menten equation of the parent model. The sigmoidal formulation permitted a higher control of Ca^{2+} uptake, in particular during the diastolic phase.

SR Ca^{2+} release (J_{rel}). The Ca^{2+} diffusion rate k_s, and the ryanodine receptors (RyRs) Ca-dependent activation rate, k_{om}, were set to 148 × 10^6 s^{-1} and 660 s^{-1}, respectively, through automatic optimization.

Ca^{2+} diffusion and Ca^{2+} buffers. The time constant for Ca^{2+} diffusion from the subsarcolemma to the cytosol (τ_{difCa}) was set to 5.469×10^{-5} s. The Ca^{2+} association constants for calmodulin (kf_{CM}) and calsequestrin (kf_{CQ}) were set to 1.642×10^6 and 175.4 (mM s)$^{-1}$, respectively. Calmodulin is involved in Ca^{2+} buffering in the cytosolic compartment, whereas calsequestrin binds Ca^{2+} in the junctional SR (jSR).

Ion concentrations

Ca^{2+} dynamics for the four compartments were described by the mass balance equations. Intracellular Na^+ was fixed at 5 mM, the Na^+ concentration in the pipette solution used in the whole cell configuration by Verkerk *et al.* (2007*b*). In such a configuration, intracellular Na^+ is expected to equilibrate with the pipette solution.

Sensitivity analysis

The sensitivity analysis was performed according to the approach proposed by Sobie (2009). The randomization procedure involved the parameters that underwent automatic optimization and the remaining maximal conductances, for a total of 18 parameters. The conductances were randomized through scaling factors chosen from a log-normal distribution with a median value of one and an SD $\sigma = 0.1873$; thus, an increase of 20% represents 1 SD away from the control value.

Shifts of the steady-state gating variables and the sarco-endoplasmic reticulum Ca^{2+}-ATPase (SERCA) pump calcium dependence were extracted from a normal distribution centered on zero, with SDs of $\sigma = 2$ mV and $\sigma = 50$ nM, respectively. The randomization was run for a population of 500 models. All of them were simulated and the corresponding AP and CaT features were computed.

Parameters and their corresponding features were collected in the $\boldsymbol{X}$ ($n \times p$) and $\boldsymbol{Y}$ ($p \times m$) matrices, respectively, where n corresponds to the number of simulations showing an auto-oscillating behaviour (< 500), p is the number of parameters and m is the number of computed features. Next, the matrix $\boldsymbol{B}$ ($p \times m$) containing the sensitivity coefficients was computed using the formula:

$$\boldsymbol{B} = (\boldsymbol{X}^{\mathrm{T}} \times \boldsymbol{X})^{-1} \times \boldsymbol{X}^{\mathrm{T}} \times \boldsymbol{Y}$$

Functional effects of mutations

Mutations in genes encoding (subunits of) ion channels may lead to changes in electrophysiological properties. We incorporated such functional effects into the model by modifying the parameters of the affected ion channel according to values reported in the literature (Tables 2–4). Only studies reporting changes in heart rate as (one of) the clinical effects of mutations were included.

The altered functionality was implemented as a shift of the steady-state (de)activation or inactivation curve, a change in its slope factor or a reduction in maximal conductance. Mutations may also cause a change in the voltage-dependent time constant (τ) curve. When changes in the time constant had been experimentally reported, they were implemented by a constant multiplication factor. Otherwise, τ underwent the same voltage shift applied to steady-state (in)activation curve.

When I_{Na} channels are incompletely inactivated, an additional non-inactivating term is added to the control formulation of I_{Na}, to reproduce a persistent, 'late' inward sodium current ($I_{Na,L}$), which is not normally present in the model. Its maximal conductance was derived from the ratio $I_{Na,L}$:I_{Na} peak, as observed experimentally.

Autonomic modulation

The effects of 10 nM ACh on I_f activation (–7.5 mV shift in voltage dependence of activation), I_{CaL} (3.1% reduction of maximal conductance) and SR Ca^{2+} uptake (7% decrease of maximum activity) were all adopted from the parent model (Severi *et al.* 2012). The administration of ACh also activates $I_{K,ACh}$, which is zero in the default model. The $I_{K,ACh}$ formulation was derived from the parent model. The maximal conductance $g_{K,ACh}$ was set to 3.45 nS (reduced by 77.5%) to achieve an overall reduction of the spontaneous rate by 20.8% upon administration of 10 nM ACh, as observed by Bucchi *et al.* (2007) in rabbit SAN cells.

The targets of isoprenaline (Iso) are I_f, I_{CaL}, I_{NaK}, maximal Ca^{2+} uptake and I_{Ks}. Changes in currents were adopted from the parent model, except for the modulation of I_{CaL}, where the effect of Iso induced a slightly smaller decrease of the slope factor k_{dL} (−27% with respect to control conditions, instead of the −31% assumed by the parent model). The I_{CaL} current was modulated to fit the experimental data reported by Bucchi *et al.* (2007) on rabbit SAN cells (26.3 ± 5.4%; mean ± SEM, $n = 7$) for the same Iso concentration.

Hardware and software

The human SAN model was built in Simulink (The Mathworks, Inc., Natick, MA, USA). Simulations ran on an OS X Mavericks (version 10.9.5) Apple computer (Apple, Cupertino, CA, USA) equipped with an Intel i7 dual core processor (Intel, Santa Clara, CA, USA). Numerical integration was performed by ode15s, a variable order solver based on numerical differentiation formulas, provided by MatLab (The Mathworks, Inc.). Simulations were run until steady-state was reached, which

Table 2. Changes introduced in the I_f model parameters to reproduce the electrophysiological characteristics of mutant *HCN4* channels, and associated clinically reported heart rate

Mutation	Type of expression	Expression system	Activation			Current density (%)	Heart rate (beats min^{-1})	Reference
			$V_{1/2}$ shift (mV)	Slope (%)	Tau shift (mV)			
G480R	Heterozygous	Oocytes, HEK	−15	–	−15	−50%	NC: 73 ± 11 C: 48 ± 12	Nof *et al*. (2007)
Y481H	Heterozygous	CHO	−43.9	NS	−43.9	NS	IP1: < 30 IP2: 40	Milano *et al*. (2014)
G482R a	Heterozygous	CHO	−38.7	NS	−38.7	NS	NC: 63 C: 48 ± 10.7	Milano *et al*. (2014)
G482R b	Heterozygous	HEK	NS	NS	NS	−65%	NC: 63 C: 41 ± 5	Schweizer *et al*. (2014)
A485V	Heterozygous	Oocytes, HEK	−30	–	−30	−66.4%	NC: 77 ± 12 C: 58 ± 6	Laish-Farkash *et al*. (2010)
R524Q	Heterozygous	HEK	+4.2	–	+4.2	NS	IP: 98.5 ± 14.2	Baruscotti *et al*. (2017)
K530N	Heterozygous	HEK	−14.2	NS	−14.2	–	NC: 74 C: 60.6 ± 6.9	Duhme *et al*. (2013)
D553N	Heterozygous	COS	NS	NS	–	−63%	IP: 39	Ueda *et al*. (2004)
S672R	Heterozygous	HEK	−4.9	NS	−4.9	–	NC: 73.2 ± 1.6 C: 52.2 ± 1.4	Milanesi *et al*. (2006)

Experimental data are changes relative to wild-type currents. These changes are used to simulate the effect of *HCN4* mutations. Oocytes, *Xenopus* oocytes; HEK, HEK-293 cells; CHO, CHO cells; COS, COS-7 cells. $V_{1/2}$ shift, shift in I_f steady-state activation curve; slope, slope factor of steady-state activation curve; tau shift, shift in voltage dependence of time constant of activation. –, not reported. NS, no significant change. Heart rate is resting heart rate in index patient (IP), mutation carriers (C), or non-affected family members (non-carriers, NC).

occurred after 50 s, based on the observation of calcium concentrations in each compartment. The automatic optimization and feature extraction were performed by custom code in MatLab 2013a. Model code is available at: http://www.mcbeng.it/en/downloads/software/hap-san.html and will also be published in the CellML Model Repository (http://models.cellml.org/).

Results

Human SAN model behaviour in basal conditions

Simulated AP and calcium transient. The simulated AP waveform reproduces the available experimental traces well (Fig. 2*A*). Indeed, most of the quantitative parameters that describe AP morphology (i.e. CL, MDP, APD_{90} and DDR_{100}) are within the mean ± SD range of the experimental ones (Verkerk *et al.* 2007*b*) (Table 5). In particular, the AP generated by the model is characterized by a CL of 814 ms, corresponding to a beating rate of 74 beats min^{-1}. However, the model presents a higher $(dV/dt)_{max}$ and overshoot (OS) and a longer APD_{20} (predicted features beyond the experimental mean ± SD range).

The simulated Ca^{2+} transient qualitatively reproduces the single experimental trace acquired by Verkerk *et al.* (2013), showing a smaller transient amplitude and longer duration compared to rabbit data. Even if the model predicts slightly lower values for both diastolic and systolic $[Ca^{2+}]_i$, the CaT amplitude (intracellular CaT amplitude; TA) is close to the experimental data (Fig. 2*B* and Table 6).

The time courses of the underlying currents, Ca^{2+} fluxes and Ca^{2+} concentrations in the four intracellular compartments are shown in Fig. 3. The main inward

Table 3. Changes introduced in the I_{Na} model parameters to reproduce the electrophysiological characteristics of mutant *SCN5A* channels, and associated clinically reported heart rate

			Activation			Inactivation						
Mutation	β subunit	Expression system	$V_{1/2}$ shift (mV)	Slope (%)	Tau shift (mV)	$V_{1/2}$ (mV)	Slope (%)	Tau	I_{Na} Late (%)	Current density (%)	Heart rate (beats min^{-1})	Reference
E161K	Yes	tsA201	+11.9	+17.9	+11.9	NS	NS	NS	–	−60	NC: 51 ± 0.6* C: 39 ± 1*	Smits *et al.* (2005)
G1406R	Yes	COS	–	–	–	–	–	–	–	−100	NC: 74 ± 2 C: 68.4	Kyndt *et al.* (2001)
ΔKPQ	No	HEK	+9.0	+26.8	+9.0	NS	NS	NS	0.60	–	NC: 76.4 C: 62.1	Nagatomo *et al.* (1998) Moss *et al.* (1995)
E1784K a	Yes	tsA201	+8.8	+78.1	+8.8	−14.4	NS	NS	1.5	–	IP: 42	Deschênes *et al.* (2000)
E1784K b	Yes	tsA201	+12.5	+32.6	+12.5	−15.0	NS	NS	1.85	−40	SND#	Makita *et al.* (2008)
D1790G	Yes	HEK	+6	+33.3	+6	−15	−6.8	x0.5	NS	–	NC: 64.9 C: 58.6	Wehrens *et al.* (2000) Benhorin *et al.* (2000)
1795insD**	Yes	HEK/Oocytes	+9.1	NS	+9.1	−9.7	NS	NS	1.4	−77.8	NC: 74.5 ± 13.5 C: 67.5 ± 16.4	Bezzina *et al.* (1999) Veldkamp *et al.* (2000)

Experimental data are changes relative to wild-type currents. These changes are used to simulate the effect of *SCN5A* mutations. Most experimental data are in the presence of the *SCN5A* channel β-subunit. HEK, HEK-293 cells; COS, COS-7 cells; tsA201, tsA201 cells; Oocytes, *Xenopus* oocytes. $V_{1/2}$ shift, shift in I_{Na} steady-state (in)activation curve; slope, slope factor of steady-state (in)activation curve; tau shift, shift in voltage dependence of time constant of activation; tau, time constant of inactivation; I_{Na} Late, persistent sodium current as percent of peak current under voltage clamp conditions. –, not reported. NS, no significant change. Heart rate is resting heart rate in index patient (IP), mutation carriers (C) or non-affected family members (non-carriers, NC). *Absolute minimum heart rate. #Sinus node dysfunction (SND) observed in 16/41 mutation carriers.

**Parameters employed for simulations were selected from two different experimental studies (Bezzina *et al.* 1999; Veldkamp *et al.* 2000). In particular, the set of parameters reported by Veldkamp *et al.* (2000) was extended with a depolarizing shift of the activation and a remarkable current density reduction as observed by Bezzina *et al.* (1999).

Table 4. Changes introduced in the I_{Ks} model parameters to reproduce the electrophysiological characteristics of mutant *KCNQ1* channels, and associated clinically reported heart rate

Mutation	Type of expression	Expression system	Activation $V_{1/2}$ shift (mV)	Activation Slope (%)	Activation Tau (%)	Current density (%)	Heart rate (beats min^{-1})	Reference
R231C	Homozygous	Oocytes	–	–	–	Voltage-dependent*	C:58.5 ± 7.7	Henrion et *al*. (2012)
V241F	Homozygous	HEK	−43.2	+52.9	–	–	IP1:30 IP2: 36	Ki *et al*. (2013)
ΔF339	Heterozygous	Oocytes	+25.0	–	–	−69.5	NC: 63 ± 3.5 C: 62.0 ± 6.6	Thomas *et al*. (2005)

Experimental data are changes relative to wild-type currents. These changes are used to simulate the effect of *KCNQ1* mutations. All experimental data are in the presence of the *KCNE1* β-subunit. Oocytes, *Xenopus* oocytes; HEK, HEK-293 cells. –, not reported. Heart rate is resting heart rate in index patient (IP), mutation carriers (C) or non-affected family members (non-carriers, NC).
*The ratio between the current density of I_{Ks} in wild-type condition and with R231C mutation ($I_{KsR231C}/I_{KsWT}$) used to simulate the voltage-dependent gain of function was estimated from Henrion *et al*. (2012).

(depolarizing) and outward (repolarizing) membrane currents are I_{CaL} and I_{Kr}, respectively (Fig. 3*C*). However, the peak amplitude of I_{tot} (Fig. 3*B*), and therefore the maximum AP upstroke velocity, is determined not only by I_{CaL}, but also by I_{NaCa} (Fig. 3*E*). Other currents are much smaller in amplitude than I_{CaL} and I_{Kr}. Yet, several are important determinants of the net ionic current during DD, and thus of CL (see below). Of note, as set out below, sinus node dysfunction can result from mutations in I_f, I_{Na} and I_{Ks}, which are among the smallest currents (Fig. 3*D*). The calcium-induced calcium release from the jSR upon calcium entry through the I_{CaL} channels is reflected by the rapid increase in J_{rel} (Fig. 3*G*) and the accompanying rapid drop in Ca_{jSR} (Fig. 3*K*). The resulting increase in Ca_{sub} (Fig. 3*I*) and Ca_i (Fig. 3*J*) generates an increase in Ca^{2+} uptake (J_{up}) (Fig. 3*H*).

Ionic currents during the DD phase. Figure 4 shows the time course of individual currents that play a relevant role during DD. The main inward currents during DD are I_{CaT}, I_f, I_{NaCa} and I_{CaL}. I_{CaT} activates before the membrane potential reaches MDP and reaches its maximal current density in the first 100 ms of DD (early DD), thus contributing to DDR_{100}, and then slowly decreases. I_f is considerably smaller than I_{NaCa} but its amplitude during DD is comparable with that of the net inward current (Fig. 4*B*, dash-dotted line). Similar to I_{CaT}, I_f starts activating when the membrane is still repolarizing and

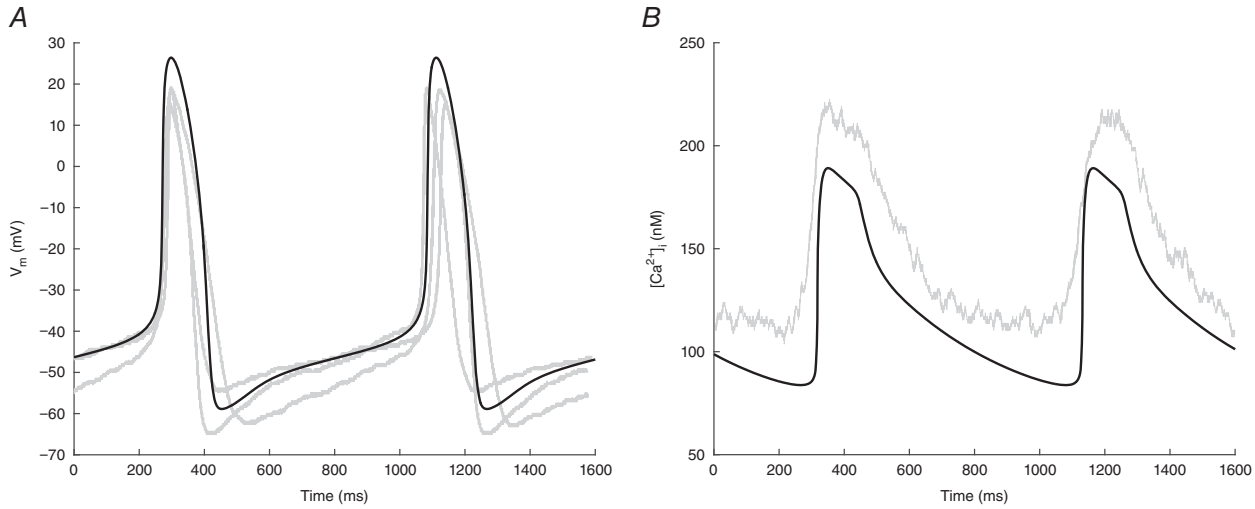

Figure 2. Action potential and intracellular Ca^{2+} transient of a single human SAN cell
A, simulated action potential of a single human SAN cell (black thick line) and experimentally recorded action potentials of three different isolated human SAN cells (grey traces). Experimental data from Verkerk *et al.* (2009*a*) and Verkerk and Wilders (2010). *B*, simulated (black thick line) and experimentally recorded (grey line) Ca^{2+} transient. Experimental data from Verkerk *et al*. (2013).

Table 5. Action potential features

AP feature	Unit	Experimental value	Present model
MDP	mV	−61.7 ± 6.1	−58.9
CL	ms	828 ± 21	814
$(dV/dt)_{max}$	V s^{-1}	4.6 ± 1.7	7.4
APD_{20}	ms	64.9 ± 23.9	98.5
APD_{50}	ms	101.5 ± 38.2	136.0
APD_{90}	ms	143.5 ± 49.3	161.5
OS	mV	16.4 ± 0.9	26.4
DDR_{100}	mV s^{-1}	48.9 ± 25.5	48.1

Comparison between experimental (mean ± SD; $n = 3$) (Verkerk *et al*. 2007*b*) and simulation data.

Table 6. Calcium transient features

Calcium transient	Unit	Experimental value	Present model
Ca_i range	nM	105–220	85–190
TA	nM	115	105
TD_{20}	ms	138.9	136.7
TD_{50}	ms	217.4	206.3
TD_{90}	ms	394.0	552.3

Comparison between experimental (Verkerk *et al*. 2013) and simulation data.

it provides its maximal contribution in the first half of diastole. I_{NaCa} is a high-density inward current; it slowly diminishes during diastole, whereas it rapidly increases at the end of DD, providing an important contribution to the AP upstroke. A small amount of fast I_{Na} window current is active during DD. It is smaller than I_f, yet it is not negligible; it is able to modulate beating rate, as demonstrated by our simulations of mutations in the sodium voltage-gated channel α subunit 5 (*SCN5A*) gene (see below). I_{CaL} follows a progressive increase during DD and becomes the major contributor to the net inward current at the end of DD; it has a relevant role during both DD and AP.

I_{NaK}, I_{Kr} and I_{Ks} are the main outward currents. I_{NaK} slowly increases during DD and reaches its maximal current density during AP, contributing to repolarization. I_{Kr} is the major driver in the repolarization process. It contributes to DD through its progressive decrease during this phase. The contribution of I_{Ks} to DD is almost negligible under control conditions, although gain-of function mutations can lead to a remarkable slowdown of pacemaking (see below).

Sensitivity analysis

Among the randomly generated population of 500 models, more than 300 showed an auto-oscillating behaviour. The results of the sensitivity analysis are reported in Fig. 5*A*, which shows the coefficients of the sensitivity matrix B, coded in a colour map. Each value in the matrix shows how a change in the parameter *P* displayed at the top is capable of affecting the feature *F* displayed on the left, and the coefficients <-0.2 and >0.2 are reported in the corresponding pixel. The obtained map highlights that nine out of the starting 18 parameters show coefficients lower or higher than the selected thresholds of −0.2 and 0.2, respectively.

As illustrated in Fig. 5*A*, changes in the permeability of I_{CaL} (P_{CaL}) and its activation kinetics (slope factor k_{dL} and shift in half-activation voltage $shift_{dL}$) have a large impact on upstroke velocity (dV/dt), AP duration ($APD_{20,50,90}$) and calcium transient. Furthermore, the kinetics of the I_{CaL} activation gate *dL* strongly affect CL and DDR_{100}. Similarly, a change of the maximal conductance of I_{Kr} (g_{Kr}) has a high impact on APA, MDP and APD, whereas the maximal activity of NCX (K_{NaCa}) strongly influences APA, dV/dt and calcium transient. Finally, a shift in the working point of the SERCA pump ($shift_{up}$) clearly affects the diastolic calcium concentration ($Ca_{i,min}$).

Figure 5*B* shows that CL is largely determined by the I_{CaL} activation kinetics (through its parameters k_{dL} and $shift_{dL}$). Figure 5*C* shows that DDR_{100} is also largely determined by the activation kinetics of I_{CaL} but in the opposite way. In addition, it reveals that the permeability of I_{CaT} (P_{CaT}) is also an important determinant of DDR_{100}.

The parameter randomization, the first step of the linear regression approach, allowed us to explore a neighbourhood, in the parameter space, of the parameter set obtained as a result of the automatic optimization procedure. Only a few parameter sets (out of 500 tested) led to comparable values of the cost function. In particular, only four led to values of MDP, CL, APD_{90} and DDR_{100} within the target range (i.e. mean ± SEM of experimental values) and only one parameter set led to a slightly lower value of the cost function than the one obtained from the 'optimized' set of parameters. To compare these two models, the effects on the pacemaking rate of mutations affecting I_f and I_{Na} were compared for the two parameter sets (as detailed in the section 'Model validation through the simulation of ion channel mutations' below). The 'alternative' set of parameters produced effects in close agreement with the 'optimized' set: the difference in mutation-induced changes in the pacemaking rate was always lower than 2.7%.

The presence of multiple parameter sets compatible with experimental ranges allowed us to compute estimation intervals for the parameters that underwent the optimization procedure (Sarkar & Sobie 2010). Nominal values and ranges for the optimized parameters are reported in Table A1 in Appendix 2.

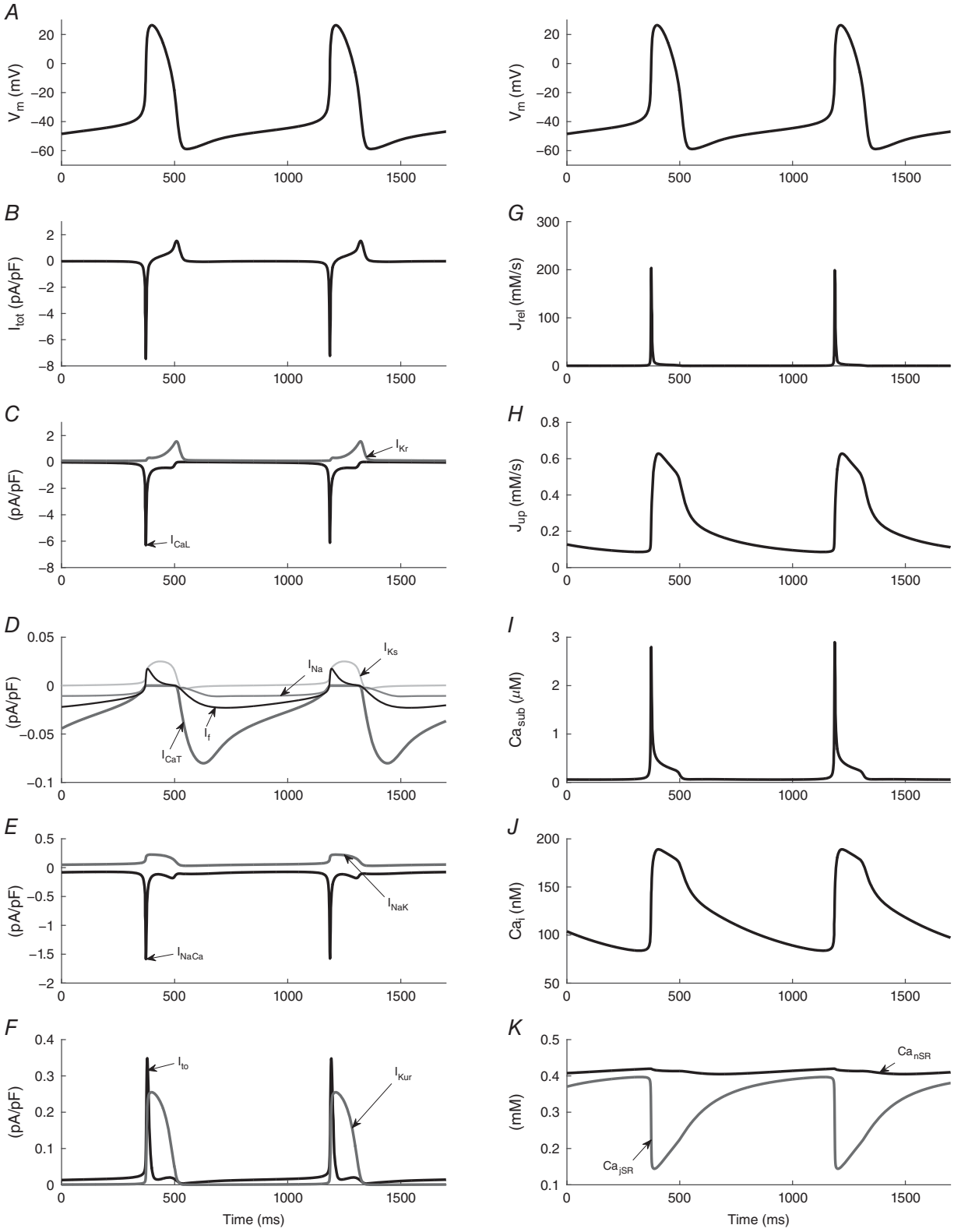

Figure 3. Time courses of simulated AP and underlying ionic currents
Simulated AP (*A*) and associated currents (*B–F*), fluxes (*G* and *H*), and calcium concentrations (*I–K*) in control steady-state conditions. Not shown is $I_{K,ACh}$, which is zero under control conditions. Note differences in ordinate scale.

To confirm that parameter values outside the estimated confidence interval lead to non-physiological (or at least non-basal) conditions, we tested the effect of changing P_{CaT} by 50% more or 50% less with respect to the parent rabbit model (instead of +15% as in the 'optimized' model). In accordance with the above observation that P_{CaT} is an important determinant of DDR_{100}, a large increase in P_{CaT} led to a notably higher beating rate (+17%; from 74 to 86 beats min^{-1}), whereas a large decrease in permeability resulted in a slower beating rate (−18%; from 74 to 60 beats min^{-1}). These results indicate that I_{CaT} could play a substantial role in pacemaking and underscore that the proposed value for P_{CaT} is quite well constrained (see also Table A1 in Appendix 2).

Model validation through the simulation of ion channel mutations

The implementation of the functional changes in ion channels as a result of genetic mutations allowed validation of the present model of the human SAN AP. A prerequisite of the validation process was that mutations included in the analysis had to be characterized both clinically and electrophysiologically. Specifically, the criteria that a mutation had to satisfy were: (i) the availability of clinical data on adult patients affected by sinus node dysfunction related to the ion channel mutation of interest and (ii) the availability of an electrophysiological characterization of the mutation, usually carried out in heterologous cell systems (COS-7, CHO, tsA201 and HEK-293 cells; *Xenopus* oocytes), into which the mutation was transfected. Furthermore, to represent the clinical conditions as faithfully as possible, the electrophysiological data were ideally obtained from systems in which the expression of the mutation was heterozygous. However, in the absence of data on heterozygously expressed gain-of-function mutations in potassium voltage-gated channel subfamily Q member 1 (*KCNQ1*), data from homozygously expressed mutations were used.

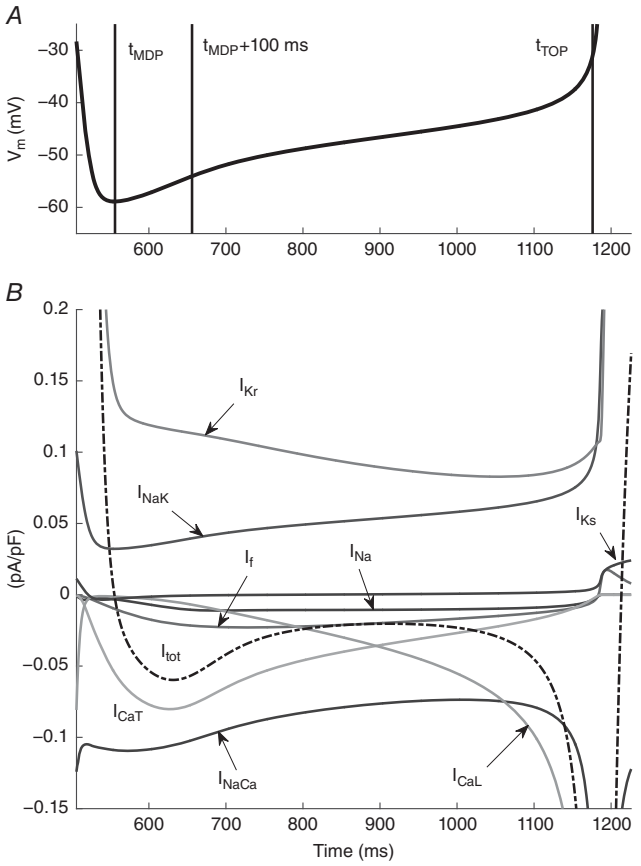

Figure 4. Membrane currents underlying diastolic depolarization
Membrane potential (*A*) and associated net membrane current (*B*) (I_{tot}, dash-dotted trace) during diastolic depolarization, as well as contributing inward and outward currents. t_{MDP} and t_{TOP} indicate the time at which V_m reaches MDP and take-off potential, respectively.

We used the data from electrophysiological studies to simulate the effects of mutations in the *HCN4*, *SCN5A* and *KCNQ1* genes, encoding the HCN4, $Na_V1.5$ and $K_V7.1$ pore-forming α-subunits of the I_f, I_{Na} and I_{Ks} channels, respectively. Next, we compared the results of our simulations with the clinical data. When clinical data relative to non-carrier family members were available, the model was tuned through autonomic modulation to reproduce the average heart rate reported for non-carriers as the control beating rate. Furthermore, if the clinical control rate was lower than the intrinsic beating rate of the model (74 beats min^{-1}), a not-null basal level of ACh was simulated, whereas a fixed percentage of the effects of isoprenaline on all its targets was simulated to obtain higher control rates. When clinical data relative to non-carriers were not available, the effects of mutations were evaluated starting from the intrinsic beating rate of the model.

Effects of I_f mutations. All the initially observed mutations in *HCN4* resulted in a loss of function of I_f (Verkerk & Wilders, 2015), although, recently, a gain-of-function mutation in *HCN4* (R524Q) has also been reported by Baruscotti *et al.* (2017). A complete list of the mutations taken into consideration in the present study, together with a short description of their electrophysiological characterization and the parameter values used in simulations, is reported in Table 2.

A loss-of-function-induced decrease in the intensity of I_f could be the result of (i) a hyperpolarizing shift of the steady-state activation curve y_∞ and time constant τ_y [e.g. for the Y481H and G482R (Milano *et al.* 2014) and the K530N (Duhme *et al.* 2013) mutations]; (ii) a reduction of the maximal conductance [e.g. for the G482R mutation (Schweizer *et al.* 2014) and the D553N mutation (Ueda *et al.* 2004)]; and (iii) both of the aforementioned changes together (e.g. for the G480R, A485V and S672R

mutations; Verkerk & Wilders, 2015). Furthermore, there can be mutation-induced changes in the activation and/or deactivation rate of the I_f channel that contribute to the decrease of I_f intensity (e.g. the slowed activation in case of the G480R mutation; Nof *et al.* 2007).

In the simulations, all three types of loss-of-function mutations led to an increase in CL and thus a reduction of pacemaking rate (Fig. 6*A*). A more detailed look at the AP features reveals that DDR_{100} showed a substantial decrease for all loss-of-function mutations, varying from 8.5% for the relatively mild S672R mutation (pacemaking rate of 69 beats min^{-1}) to 40.7% for the A485V mutation (pacemaking rate of 61 beats min^{-1}), whereas APD_{90} was almost unchanged in our simulations. Similarly, changes in MDP and APA were almost negligible: the maximum hyperpolarization of the MDP amounted to 0.5 mV and the maximum increase in APA was 0.9 mV (both for the A485V mutation).

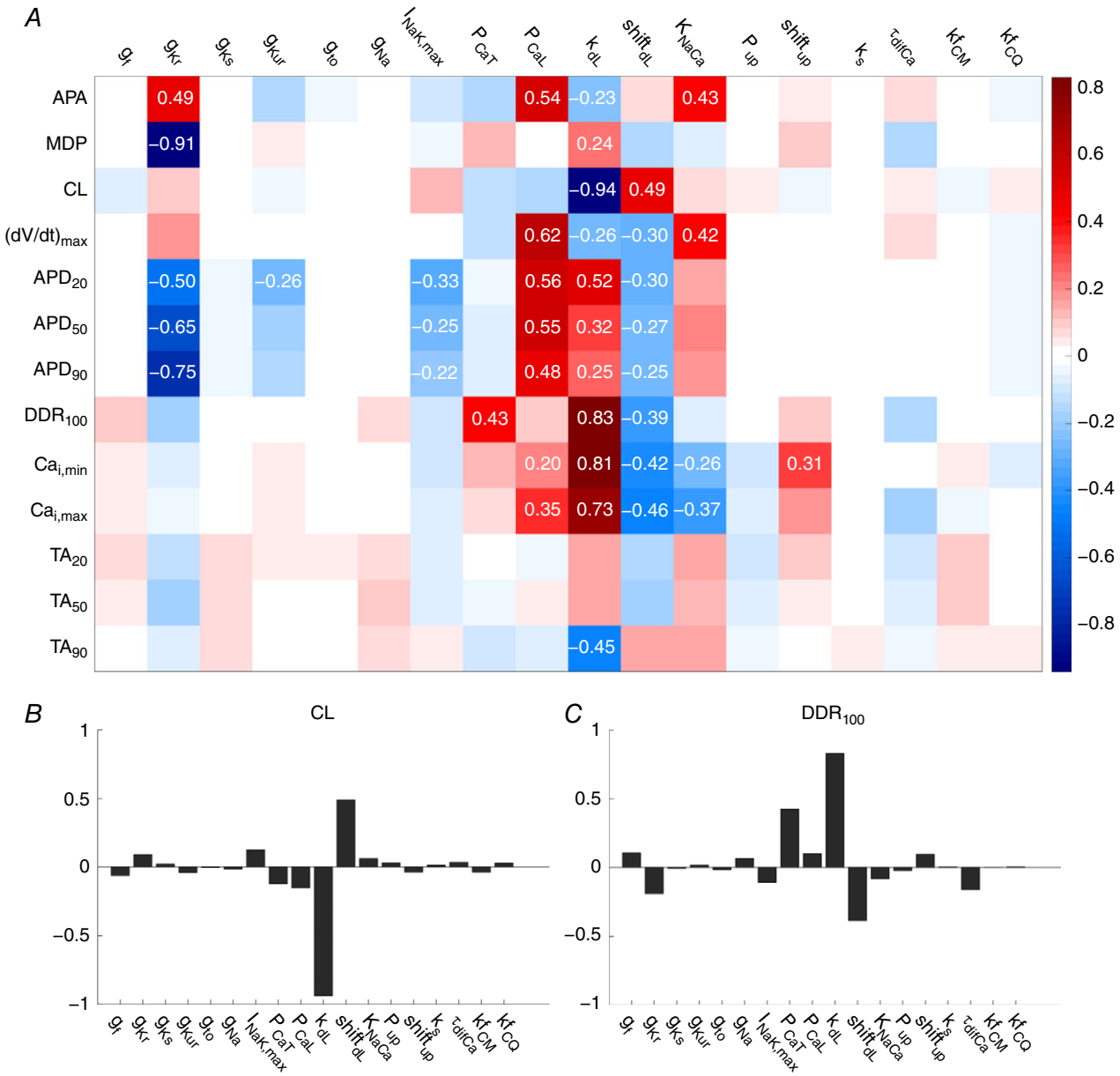

Figure 5. Sensitivity analysis
A, colour coded map of sensitivity matrix *B*. Columns show how a specific parameter *P* affects AP and CaT features; rows show how each feature is affected by different parameters. Red, blue and white pixels represent positive, negative and no substantial correlation, respectively, between parameters and features. Coefficients < -0.2 or > 0.2 are considered substantial. *B* and *C*, graphs indicating how changes in each of the parameters affect CL and DDR_{100}. The two panels display the information reported in rows 3 and 8 of (*A*) in different ways.

The only gain-of-function mutation, R524Q, led to an increase in I_f by shifting the steady-state activation curve and the time constant curve towards less negative potentials (Baruscotti *et al.* 2017). The simulation of the mutation showed a faster pacemaking rate (79 beats min^{-1}). DDR_{100} had an increase of 8.2%, whereas MDP, APD_{90} and APA were unchanged.

The comparison between the pacemaking rates in our simulation data and the clinically observed heart rates (Fig. 6*A*) highlighted the ability of the model to reproduce the effects of the mutations on *HCN4* channels, at least qualitatively. Quantitatively, the effects in the simulation data are consistently smaller than those observed clinically, which might be expected (see Discussion).

Effects of I_{Na} mutations. A large number of mutations identified in *SCN5A* are related to sinus dysfunction, such as sinus bradycardia and sinus pauses (often associated with the LQT3 phenotype) and sick sinus syndrome (Veldkamp *et al.* 2003; Lei *et al.* 2007).

A loss of function of the I_{Na} channel can have several causes: (i) a rapid inactivation of the ion channel; (ii) a depolarizing shift of activation; (iii) a hyperpolarizing shift of inactivation; and (iv) a reduction of the current density, which, in some cases, can lead to the non-function phenotype (i.e. a full loss of function). In several cases, multiple causes can be present at the same time, enhancing the reduction of I_{Na} (Table 3).

The simulations of the effects of loss-of-function I_{Na} mutations showed a decrease in pacemaking rate, up to 11.8% for the E161K mutation. DDR_{100} showed a decrease for all mutations (with a maximum of 9.0% for E161K). APD_{90}, MDP and APA were almost unchanged for all mutations.

In simulations of ΔKPQ (Nagatomo *et al.* 1998) and E1784K [parameters from Deschênes *et al.* (2000) or Makita *et al.* (2008)] and 1795insD mutations [parameters from Bezzina *et al.* (1999) and Veldkamp *et al.* (2000)], an incomplete inactivation (gain of function) was combined with a loss of function; the absence of a complete

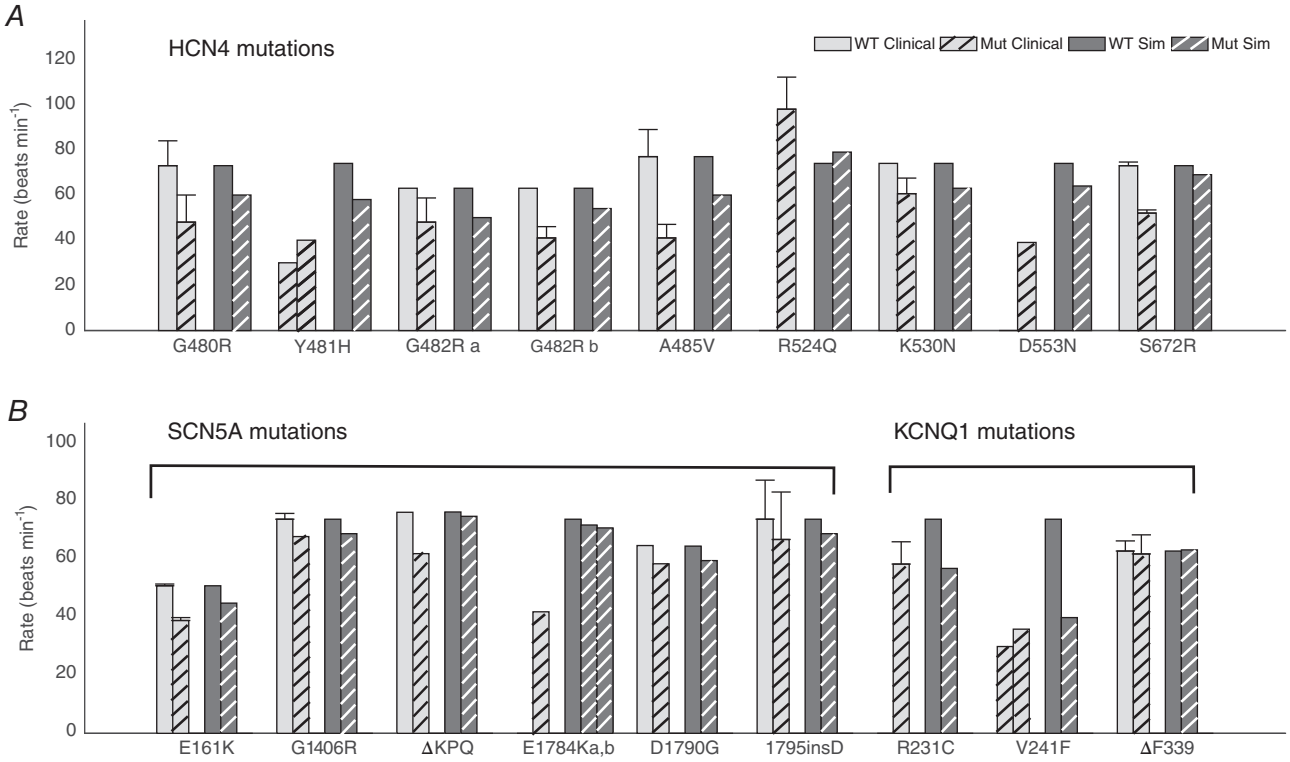

Figure 6. Clinically observed *vs.* simulated effects of I_f, I_{Na} and I_{Ks} mutations
A, comparison between clinical data (solid and hatched light grey bars) and simulation data (solid and hatched dark grey bars) on the effects of mutations affecting *HCN4* channels (I_f). For the Y481H, R524Q and D553N mutations, no clinical data from non-carrier family members were available. SDs of the clinical data, where available, are indicated. *B*, comparison between clinical data (solid and hatched light grey bars) and simulation data (solid and hatched dark grey bars) on the effects of mutations affecting *SCN5A* channels (I_{Na}, group on the left) and *KCNQ1* (I_{Ks}, group on the right). SDs of the clinical data, where available, are indicated. For the E1784K (a) mutation, no clinical data from non-carrier family members were available. Clinical data on the E1784K (b) mutation were only reported in a qualitative way ('sinus node dysfunction') (Table 3). For the R231C and V241F mutations, no clinical data from non-carrier family members were available. SDs of the clinical data, where available, are indicated.

inactivation induced a sustained (late) Na^+ current. The DDR_{100} resulting from this combined gain and loss of function showed a decrease (−5.8% for ΔKPQ, −7.9% and −7.7% for E1784K, and −8.0% for 1795insD mutation). By contrast, APD_{90} showed an increase for all three mutations (+1.3% for ΔKPQ, +2.2% and +1.5% for E1784K, and +0.6% for 1795insD mutation). The overall effect was a reduction of the pacemaking rate for all simulated mutations (by −4.8% for ΔKPQ, −2.9% and −3.7% for E1784K, and −6.2% for 1795insD mutation). To assess the contribution of an incomplete inactivation of I_{Na} channels in these 'mixed mutations', we investigated the effect of I_{NaL} alone by introducing this current into a cell in control conditions. The presence of I_{NaL} caused two opposing effects: enhanced inward current during late DD resulted in a steeper DDR, whereas inward I_{Na} current during AP prolonged APD. In our model for g_{NaL} set to 1% of g_{Na} in the control condition, the higher inward current during late DD prevailed. The overall effect of I_{NaL} was a minor increase of the pacemaking rate (+3.2%). However, in the four mixed mutations analysed, the loss-of-function effect prevailed and led to an overall slowdown of the pacemaking rate.

A comparison of pacemaking rates predicted by the model and clinical data is shown in Fig. 6*B*. The simulation data for the G1406R, D1790G and 1795insD mutations were in close agreement with the clinical data. By contrast, for the other three mutations, the simulations showed a decrease of the beating rate compatible with the loss-of-function behaviour of the mutations, although it was less close to the clinically observed effect.

Effects of I_{Ks} mutations. Both loss-of-function and gain-of-function mutations in *KCNQ1*, encoding the $K_V7.1$ pore-forming α-subunit of the I_{Ks} channel, have been reported in relation to sinus bradycardia.

A gain of function of $K_V7.1$ channels could be the result of (i) a higher current density, as observed for the R231C mutation (Henrion *et al.* 2012) or (ii) a hyperpolarizing shift of the steady-state activation curve, as observed for the V241F mutation (Ki *et al.* 2013). With either mutation, DDR_{100} was markedly increased. However, the overall DDR was reduced, leading to a longer DD phase duration. Both mutations showed a slight depolarization of MDP (to −57.6 and −57.1 mV for R231C and V241F, respectively), whereas APD_{90} was considerably reduced (by 10.8% and 19.8% for R231C and V241F, respectively). Thus, opposing effects were present. However, the prolongation of the DD phase far outweighed the effects of a higher DDR_{100} and a shorter APD_{90}, leading to slower pacemaking rates (57 and 40 beats min^{-1} for R231C and V241F, respectively), which were in good agreement with clinical data (Fig. 6*B*).

On the other hand, a loss of function of $K_V7.1$ channels can be attributed to (i) a lower channel expression or (ii) a depolarizing shift of the steady-state activation curve. The ΔF339 mutation shows both effects (Table 4) (Thomas *et al.* 2005). The model predicted a negligible change in pacemaking rate (from 63 to 63.5 beats min^{-1}), which is consistent with clinical data (Fig. 6*B*); DDR_{100} was slightly reduced (by 2.4%) and APD_{90} was increased (by 1.3%), whereas MDP was almost unchanged.

Model-based analysis: effects of I_f and Ca^{2+} handling modulation on pacemaking

Contribution of I_f to pacemaking. To quantitatively assess the sensitivity of CL, and thus of pacing rate, to the funny current, we carried out two simulation experiments: (i) a progressive block of funny current, by reducing the maximal conductance g_f and (ii) a shift in voltage dependence of the steady-state activation curve, with a range from −15 to +15 mV.

Four levels of block were assessed: 30%, 70%, 90% and 100% (i.e. full block) (Fig. 7*A*). The total block of funny current led to an increase in CL of 28.1% to 1043 ms, and thus a decrease in pacemaking rate of 22% to 58 beats min^{-1}, in good accordance with the 26% increase in CL that was experimentally observed by Verkerk *et al.* (2007*b*), who administered 2 mM Cs^+ as a blocker of I_f to a single isolated SAN cell (Fig. 7*B*). At this concentration, Cs^+ almost completely blocks I_f in the pacemaker range of potentials, whereas the delayed rectifier K^+ current, which is also sensitive to Cs^+, is only affected slightly (Denyer & Brown, 1990; Zaza *et al.* 1997; Liu *et al.* 1998).

The increase in CL was mainly the result of a lower DDR and longer DD phase (with DDR_{100} decreasing by 39.7% to 29 mV s^{-1} upon full block), whereas APD_{90} and MDP remained almost unchanged (Fig. 7*A*). Of note, the increase in CL was also largely the result of a lower DDR and longer DD phase in the experiment of Verkerk *et al.* (2007*b*) (Fig. 7*B*).

Negative shifts of the activation led to an increase in CL, up to 957 ms (+17.5% with respect to control) with a −15 mV shift, whereas positive shifts shortened CL, up to 577 ms (−29.2%) with a +15 mV shift (Fig. 8*A*). As with the I_f block, DDR_{100} was the main descriptive parameter that changed (to 37.7 mV s^{-1} (−25.8%) with a −15 mV shift and to 75.4 mV s^{-1} (+56.8%) with a +15 mV shift; Fig. 8*B*), whereas APD_{90} and MDP remained almost unaffected, as for the I_f block (Fig. 8*C* and *D*).

Contribution of I_{NaCa} to pacemaking and spontaneous calcium oscillations. The Na^+/Ca^{2+} exchanger is an important actor in the generation of the AP and also contributes to the diastolic depolarization phase. To assess the impact that I_{NaCa} has on CL, we performed a progressive reduction of the maximal activity of Na^+/Ca^{2+} (K_{NaCa}) (Fig. 9).

Reductions in K_{NaCa} of 50% and 75% unexpectedly led to faster pacemaking, with a rate of 83 beats min^{-1}

(+12.2%) and 93 beats min^{-1} (+25.7%), respectively. DDR_{100}, APD_{90} and MDP contributed synergistically towards a shorter CL: DDR_{100} increased remarkably, APD_{90} shortened and MDP depolarized (Fig. 9*A*). DDR_{100} was steeper as a result of a more intense I_{NaCa} density during DD (Fig. 9*B* and *D*) because of a higher concentration of $[Ca^{2+}]_i$ in the cell (Fig. 9*C*). The reduced maximal activity of the Na^+/Ca^{2+} exchanger also resulted in a lower contribution of I_{NaCa} to the AP: the overshoot potential was lower and repolarization was faster, resulting in a shorter APD.

Higher levels of block of the exchanger (reduction of maximal activity by 90%) stopped the automaticity of the cell. The inward current provided by the Na^+/Ca^{2+} exchanger was no longer sufficient to make the cell reach its threshold potential for an AP. Membrane potential stabilized at a level approaching –40 mV (Fig. 9*A* and *B*), whereas $[Ca^{2+}]_i$ stabilized at a constant value close to 200 nM (Fig. 9*C*).

The presence in the model of the 'isolated Ca^{2+} oscillator' was also tested, by reproducing the simulations in which all membrane currents are set to zero. Spontaneous oscillations of intracellular and sub-sarcolemmal calcium were indeed achieved upon a large increase in the SERCA pump activity. Notably, the frequency of these oscillations was definitely higher than the physiological human heart rate (> 5 Hz). In particular, calcium oscillations were not sustained for P_{up} values up to more than 90 nM s^{-1}; sustained oscillations, with a frequency of ≈5 Hz, arose upon increasing P_{up} to a value approaching 100 nM s^{-1}. This frequency stayed almost constant as P_{up} was increased to 120 mM s^{-1}, suggesting that it might be not easy to tune the oscillation rate in a robust way, at least in this lumped-parameter model of calcium handling.

Autonomic modulation of pacemaking

The simulated administration of 10 nM ACh resulted in a reduction of spontaneous rate by 20.8%. DDR_{100} was decreased by 9.8% and APD_{90} was shortened from 161.5 to 154 ms (−4.6%); MDP was not altered. Even though ACh had opposing effects on DDR_{100} and APD_{90}, the increase in CL showed that the DDR_{100} reduction prevailed (Fig. 10*A*).

We also assessed the contribution of each individual ion current by applying the ACh effect to each current separately. Changes in $I_{K,ACh}$ and I_f were dominant, inducing a reduction in the pacemaking rate of 11.6% and 6.9%, respectively. Exposure of only I_{CaL} to ACh resulted in a minor effect (1.1% reduction of pacemaking rate), whereas the modification of J_{up} led to negligible changes. Simulating the ACh effects on all targets but one led to similar results: $I_{K,ACh}$ and I_f played a primary role, as demonstrated by the model-predicted reduction of the pacemaking rate by 8% and 13% (when $I_{K,ACh}$ and I_f were the only unchanged currents), respectively.

The overall effect induced by 1 μM Iso resulted in an increase in the pacemaking rate of 27.9% to 94 beats min^{-1} (Fig. 10*A*). DDR_{100} increased from 48.1 mV s^{-1} in control conditions to 53.4 mV s^{-1} with Iso, whereas APD_{90} and MDP were almost unchanged.

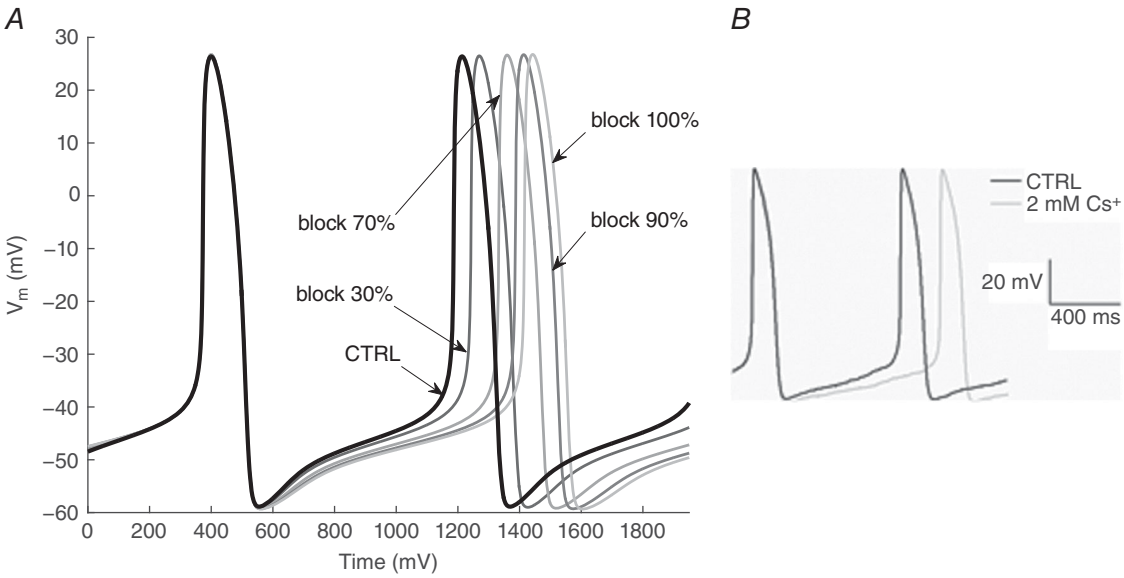

Figure 7. Functional effect of I_f block
A, simulated AP under control conditions (CTRL) and upon 30%, 70%, 90% and full block of I_f. *B*, effects of administration of Cs^+ (2 mM) on the AP of an isolated human SAN myocyte. Experimental trace adapted from Verkerk *et al*. (2007*b*).

The assessment of the effect of Iso through each of the Iso-sensitive currents alone showed that the modified I_f and I_{CaL} both led to a substantial increase in pacemaking rate (14.2% and 16.4%, respectively). The increased activity of I_{NaK}, on the other hand, slowed the pacemaking rate (−13.1%), whereas Iso-induced changes in I_{Ks} and J_{up} only had a small effect (+1.5% and −0.4%, respectively).

Considering the effects of all currents but one confirmed the above results; when all the currents but one, either I_{CaL}, I_f, I_{NaK}, I_{Ks} or J_{up}, were affected by 1 μM Iso, an increase in beating rate equal to 2.1%, 9.6%, 40.6%, 21.3% and 28.7%, respectively, was observed. Of note, these values also show that I_{Ks} becomes more prominent at higher rates, when there is less time for its deactivation. The effect of I_{Ks} alone is small, with a 1.5% increase in beating rate, although the 'all but one' data (21.3% increase) reveal a more prominent role of I_{Ks} at higher rates; indeed, the net contribution of I_{Ks} (overall effect – all but I_{Ks} effect) shows an increase of beating rate equal to 6.6% (27.9–21.3%).

The model was capable of reproducing the full clinical range of human heart rate, assumed to be from 40 to 180 beats min^{-1}. In particular, the model predicted that a concentration of ACh equal to 25 nM was able to slow down the pacemaking rate to 40 beats min^{-1} (−45.9%). This concentration was responsible for a negative shift of the (de)activation steady-state curve y_∞ and time constant τ_y of −6.3 mV, a reduction of P_{CaL} equal to −6.7% and a maximal activity of SERCA pump P_{up} reduced to 85% with respect to control conditions. The $I_{K,ACh}$ was also affected, showing a peak value of 0.33 pA/pF. The model

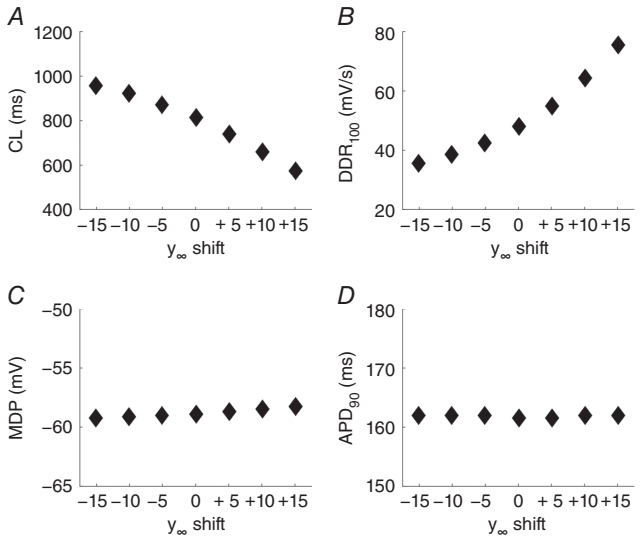

Figure 8. Functional effect of changes in voltage dependence of I_f activation
Simulations of the effect of −15 to +15 mV shifts (with steps of 5 mV) in voltage dependence of the y_∞ steady-state activation curve of the funny current on (*A*) cycle length, (*B*) DDR_{100}, (*C*) MDP and (*D*) APD_{90}.

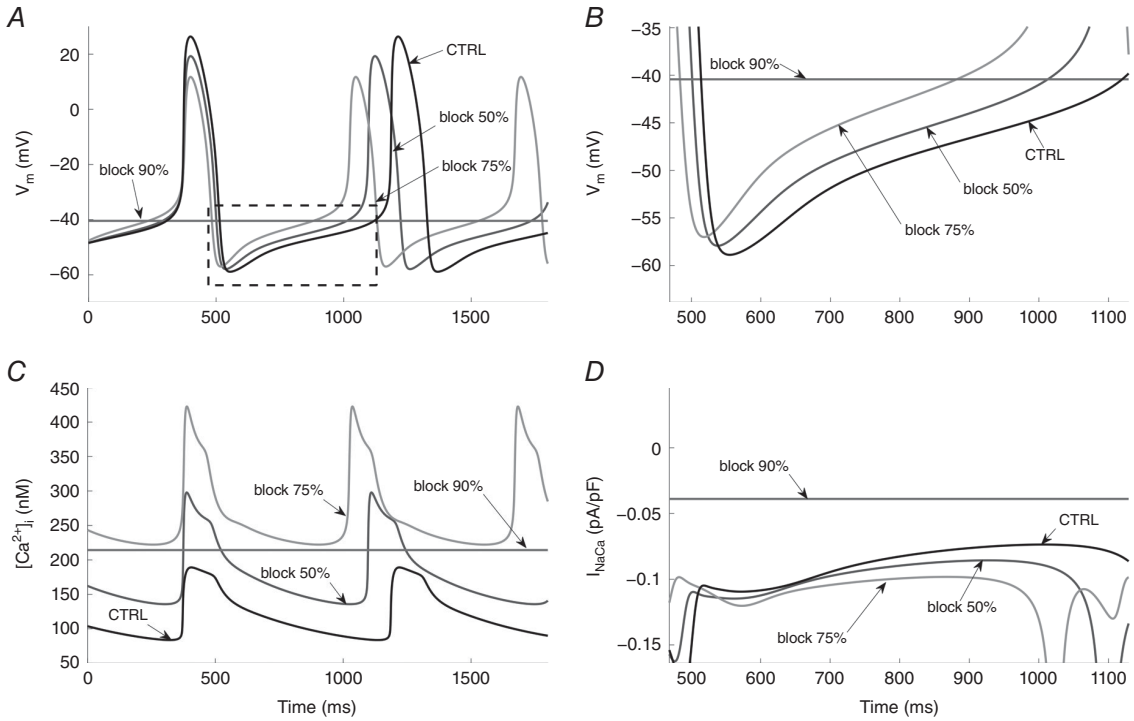

Figure 9. Functional effect of I_{NaCa} block
Simulated AP (*A*) and associated $[Ca^{2+}]_i$ time course (*C*) under control conditions (CTRL) and upon 50%, 75% and 90% block of I_{NaCa}. Simulated AP (*B*) and associated I_{NaCa} time course (*D*) relative to the dashed box of (*A*).

also showed stable oscillations at a pacing frequency equal to 182 beats min^{-1}. Changes in the Iso target parameters responsible for this pacemaking rate were quantified (with respect to control conditions) as: y_∞ and τ_y were shifted by +12 mV; $I_{NaK,max}$ and g_{Ks} were increased by 92%; and n_∞ and τ_n were shifted by −22 mV. I_{CaL} was affected by a 96.8% increase of P_{CaL}, a shift of dL_∞ and τ_{dL} by –12.8 mV, and a slope factor k_{dL} reduced by −29.7%. Thus, we directly tuned the parameters affected by Iso, increasing the aforementioned effects of 1 μM Iso to arrive at a pacemaking rate approaching 180 beats min^{-1}.

Discussion

In the present study, we formulated a comprehensive human SAN AP model, starting from a state-of-the-art model of rabbit cardiac pacemaker cells, and converting it into a species-specific description using human experimental data as far as possible. A novel aspect is the adoption of an automatic optimization procedure, tightly bounded by the AP features, to identify the parameters for which experimental data are presently unavailable.

Previously, Chandler *et al.* (2009) showed that scaling ion current densities, according to the gene expression pattern they found in human SAN *vs.* atrial tissue, gives rise to automaticity in the human atrial cell model of Courtemanche *et al.* (1998). However, the values of the descriptive parameters of AP, in particular MDP, APA and APD, were far from the experimentally observed ones.

Our model is able to reproduce the main experimentally observed electrophysiological features (AP waveform, calcium transient) and the simulated changes in pacemaking rate as a result of mutations affecting ionic channels are in line with clinical data. Furthermore, it allows the investigation of relevant conditions such as I_f block, NCX block and autonomic stimulation, as we have demonstrated above.

Construction of the model

AP models of cardiac cells are commonly based on voltage clamp data for ionic current identification and current clamp data for model validation. We tried to maximally exploit the scarce data available on human SAN

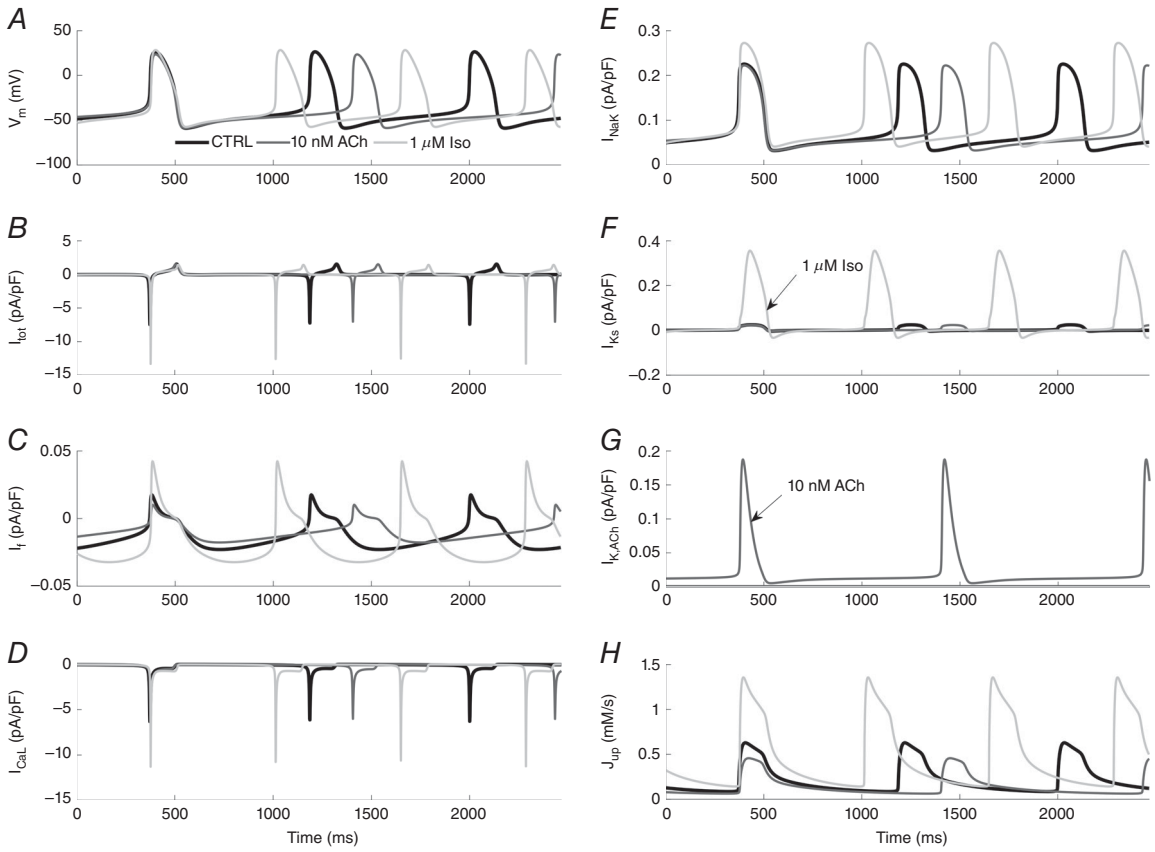

Figure 10. Functional effect of ACh and isoprenaline
Time course of (*A*) membrane potential, (*B*) net current, target currents (*C*–*G*) and SERCA-pump uptake (*H*) in control conditions (CTRL, black lines), upon administration of 10 nM ACh (dark grey lines) and 1 μM Iso (light grey lines). Targets for ACh are I_f, I_{CaL}, $I_{K,ACh}$ and J_{up}; targets for Iso are I_f, I_{CaL}, I_{NaK}, I_{Ks} and J_{up}. Note the differences in ordinate scales.

cells, aiming at a detailed reproduction of experimental AP morphology. Updating the description of the funny current, based on the experimental data obtained by Verkerk *et al.* (2007*b*), was also crucial. In our human cell model, I_f current density during DD is considerably lower than in rabbit SAN cells, although it remains comparable to the net inward current as reported by Verkerk and Wilders (2010) in their virtual AP clamp experiments.

In control conditions, the model reproduces the experimental AP features well. The simulated AP is characterized by CL = 814 ms, which is close to the experimentally observed values (Verkerk *et al.* 2007*b*) and critical parameters such as MDP, APD_{90} and DDR_{100} are all within the range of the experimental data (Table 5). As a consequence, the model shows a representative behaviour during both DD (subthreshold) and AP (Fig. 3).

To achieve a calcium transient close to the experimental trace, several actors of Ca^{2+} handling underwent changes; in particular, maximal NCX activity was reduced by 53%, and a sigmoidal equation was introduced to describe SR uptake. These updates allowed a higher diastolic $[Ca^{2+}]_i$ and finer control during DD.

The Cs^+-induced CL prolongation that was experimentally observed was also taken into account to tune parameters. Simulating the administration of 2 mM Cs^+ led to an increase in CL of 28.1%, close to the experimentally observed 26% (Fig. 7). This Cs^+ concentration was reported to selectively and almost fully block the funny current (Verkerk *et al.* 2007*b*) and so the reported prolongation established the maximal extent of the contribution of I_f to the pacemaking rate decrease in our model. Thus, the experimentally observed levels of I_f block by Cs^+ were highly relevant. Accordingly, we should not forget that a voltage-dependent partial block of funny channels by 5 mM Cs^+ has been reported elsewhere (DiFrancesco *et al.* 1986). If the parameters in our model were tuned to reproduce a similar partial Cs^+-induced block, a larger effect of complete I_f block would be observed in simulations.

Sensitivity analysis

The sensitivity analysis highlighted the strong impact of I_{CaL}, in particular its activation kinetics (gate *dL*), on CL and on the calcium transient. A slight increase/decrease of the slope factor k_{dL} and a shift of the working point of the steady-state curve of the activation gate are able to substantially change these two features; indeed, the availability of open I_{CaL} channels during the highly sensitive DD phase is strongly affected by slight changes of the *dL* kinetics.

The same AP can be produced by multiple sets of parameters. However, the observation that only a few parameter sets, out of a total of 500, produced simulation data within the experimental range suggests that the parameters should fall within a narrow range. Ranges in Table A1 in Appendix 2 are a first attempt to determine such physiological intervals for human SAN cells exploiting the limited experimental data. Future measurements will help to refine the information extracted by our investigation.

The illustrative investigation on the effects of changes in P_{CaT} suggests that this parameter is well constrained, and also that I_{CaT} plays a role in pacemaking, which is consistent with the report by Mangoni *et al.* (2006) who studied mice with a disrupted gene coding for $Ca_V3.1$ channels, as responsible for T-type calcium current.

Ion channel mutations

Having obtained satisfying behaviour in control conditions, we further validated the model through the implementation of mutations affecting ion channels. Because of the clinical importance of this research, a large number of studies have previously been carried out and a considerable amount of both clinical and electrophysiological data are available. *HCN4* is the most abundant isoform of the HCN family. Most *HCN4* mutations result in a loss of function of I_f, although, recently, Baruscotti *et al.* (2017) found a mutation that results in a gain of function. In our simulations, I_f exerted its contribution during DD, influencing the amount of net inward current, and thus the slope of this phase. In this way, a loss of function of I_f leads to a slower rate, whereas a gain of function leads to a faster one. A remarkable aspect of this finding is that I_f is able to modulate DDR at the same time as leaving other important parameters (such as APD and MDP) unchanged.

The simulations of loss-of-function mutations in *HCN4* show a considerable slowing but not a complete cessation of pacemaker activity. The slowing is consistently smaller than that observed in the associated mutation carriers (Fig. 6). The difference between clinical and simulated effects of mutations, however, is to be expected because the hyperpolarizing effect of the surrounding atrium will result in a more prominent role of I_f in the SA node of the intact heart. Of note, our current model appears to be more promising for assessing the effects of *HCN4* mutations in humans than the comprehensive rabbit SAN cell models described by Maltsev and Lakatta (2009) and Severi *et al.* (2012). As recently reported by Wilders and Verkerk (2016), the mutation effects appear to be highly underestimated in the Maltsev–Lakatta model, in which a slowing of only 5.2% was observed for the most severe of the 11 mutations tested (A485V; 21.4% in the present model) and highly overestimated in the Severi–DiFrancesco model, where pacemaker activity ceased for five of the 11 mutations, including A485V.

In the validation stage, a large number of mutations in the *SCN5A*-encoded $Na_v1.5$ channels were assessed. We observed two kinds of mutations: the first kind

was characterized by changes in electrophysiological properties that led to a loss of function of channels (E161K, G1406R and D1790G); the second kind showed the concurrent presence of loss of function and gain of function (ΔKPQ, E1784K and 1795insD). The latter effect was the result of an incomplete inactivation of I_{Na} channels, which was incorporated into the model by means of the $I_{Na,L}$ current.

Loss-of-function mutations reduced the inward current carried by I_{Na} and therefore decreased DDR. Thus, I_{Na} regulated heart rate in a way analogous to that of the funny current; however, the lower weight of I_{Na} in the overall inward current resulted in quantitatively fewer extensive effects with respect to I_f.

Similar to the mutations in *HCN4*, the slowing in pacemaking rate associated with mutations in *SCN5A* is consistently smaller in simulations than in the intact heart (Fig. 6). Again, this is to be expected because the hyperpolarizing effect of the surrounding atrium will also result in a more prominent role of I_{Na} in the SA node of the intact heart. In our current model, we observed a decrease in the pacemaking rate of up to 14.9% for the most severe *SCN5A* mutation. We could not test the *SCN5A* mutation effects in the Maltsev–Lakatta rabbit SAN cell model because this model lacks I_{Na}. In the Severi–DiFrancesco rabbit SAN cell model, the decrease in pacemaking rate was almost negligible for each of the *SCN5A* mutations tested, with a maximum near 1%.

The simulated effect of the ΔF339 loss-of-function mutation in *KCNQ1* that affects $K_V7.1$ channels is almost negligible. The gain of function of I_{Ks} was more critical. The increase in outward current resulted in a DDR reduction that far outweighed the accompanying APD reduction. Thus, the gain-of-function mutations R231C and V241F resulted in a rate slowdown compatible with the clinically observed sinus bradycardia. However, it should be noted that the electrophysiological characterizations of both R231C and V241F were obtained in homozygous expression (Table 4). Although no experimental data are available concerning the R231C and V241F mutations in heterozygous expression, we decided to include these simulations anyway to provide a lower limit of the beating rate that the model can achieve for these mutations.

The comparison between clinical findings and simulated effects of mutations on beating rate showed good overall behaviour of the model. Except for the I_{Ks} ΔF339 mutation, simulated effects on beating rate were in accordance with the reported clinical data (Fig. 6). It should be noted that there is always a gap between clinical and simulated mutation effects, given the difference in the systems analysed: the heart rate is a macroscopic phenomenon, resulting from the overall SAN tissue behaviour and its interaction with the autonomic nervous system, whereas the beating rate predicted by the model considers only the microscopic single cell level. At this level, there is (for example) no hyperpolarizing effect of the surrounding atrium, which may increase I_f and I_{Na} and thus the functional effects of mutations in the associated genes. It should also be noted that carriers of the same mutation may show widely different phenotypes, even within the same family. This holds in particular for the *SCN5A* mutations; it is possible that only a minority of the affected family members show sinus node dysfunction. Finally, other factors, such as physical training level, can affect the difference in basal heart rate found between healthy subjects and mutation carriers.

As emphasized by Verkerk and Wilders (2015) for *HCN4* mutations, although it can be readily extended to other ion channels, there are inconsistencies between clinical and experimental data. Many factors can underlie these inconsistencies: (i) data on current density can be misleading because heterologous systems (*in vitro*) can express different levels of the gene affected by the mutation with respect to the subject (*in vivo*) under investigation; (ii) experimental data can be incomplete and may strongly depend on the expression system and the experimental protocol employed; (iii) clinical data are often limited to a small number of patients, or even a single patient; (iv) the affected isoform is not the only one expressed *in vivo*; and (v) remodelling processes can occur in mutant carriers and affect their clinical phenotypes.

Physiological insights from simulations

Simulating I_f and NCX blocks and autonomic stimulation provided insights into the model behaviour and shed light on underlying phenomena.

Lower levels of I_f block and shifts of the steady-state activation curve were able to modulate pacemaking rate, mainly by varying DDR_{100}. By contrast, MDP and APD_{90} showed no changes (Figs. 7 and 8). These results suggest that I_f exerts its capability to modulate beating rate during the DD phase. As previously shown for the rabbit SAN AP, controlling the steepness of early DD is an efficient way of determining beating rate: small changes in currents are able to substantially modify the slope of DD, and thus the overall duration of the AP. This is even more true in human SAN because the pacing rate is even more sensitive to changes in DD slope. As a result of the non-linear relationship between dV/dt and time (Zaza, 2016), the same change in current is bound to produce larger changes in CL when basal CL is longer. Unlike the parent model, pacemaker activity does not cease when I_f is fully blocked. Yet, the modulatory role of I_f is as important as in the parent model.

NCX provided an important contribution to automaticity, both during DD and during the AP upstroke. The considerable reduction of its maximal activity relative to the parent model, consistent with the gene expression

pattern reported by Chandler *et al.* (2009), allowed $[Ca^{2+}]_i$ to reach a value closer to experimental values. The NCX block showed two different effects: for low-to-moderate levels of block, the beating rate became faster than under control conditions, whereas for high-to-almost-full block, the automaticity stopped (Fig. 9). The latter result is consistent with experiments showing an inhibitory effect of Na^+ replacement by Li^+, thus abolishing NCX, on spontaneous beating in rabbit SAN cells (Bogdanov *et al.* 2001). The unexpected effect of rate acceleration upon low-to-moderate block can be the result of a counter-intuitive, although physiological, process: a lower maximal NCX activity results in a higher $[Ca^{2+}]_i$ during DD and, consequently, a more intense I_{NaCa}. Nevertheless, the rate increase induced by I_{NaCa} reduction is actually a prediction of our model, and experimental data (not available yet) are needed to confirm this prediction in human SAN cells.

Unlike I_f modulation, NCX block affected several main features: DDR_{100}, MDP, APD_{90} and even APA underwent considerable changes (Fig. 9). Of note, both the absolute and relative amplitude of I_f and I_{NaCa} during DD were highly similar to those predicted by Verkerk *et al.* (2013) through numerical reconstruction.

It is worth noting that the 'calcium clock' was integrated in the parent model and it is also present in this human model but, as expected, the NCX current cannot effectively modulate the pacemaking rate. Based on the rabbit model simulations, the SERCA pump activity could be expected to modulate pacemaking rate. This was not the case in our model, in which changes in SERCA maximal activity had a negligible effect on rate. This leaves open the question about the actual relevance of the 'calcium clock' in human SAN.

The adopted calcium handling considered the presence of a subsarcolemmal space, which is also present in the rabbit SAN cell models of Kurata *et al.* (2002), Maltsev and Lakatta (2009) and Severi *et al.* (2012). Because T-tubules are poorly defined in SAN cells, this subsarcolemmal space is proposed as a 'fuzzy space' (Lederer *et al.* 1990). NCX1 and RyRs are co-located there, as reported by Lyashkov *et al.* (2007), who used immunolabelling techniques and confocal imaging. Through further simulations, we tested the effect of a different cell arrangement of RyRs in the cell space. We progressively switched the SR release from the subspace to the cytosol until a 100% Ca^{2+} release, targeted to the cytosol and sensitive to Ca_i instead of Ca_{sub}, was reached. The model did not show dramatic changes; in an SR release configuration fully targeted to cytosol, we only observed a minor change of pacemaking rate (+5.2%; from 74 to 78 beats min^{-1}), as well as a minor increase in Ca_i ($Ca_{i,min}$ from 84 to 99 nM, $Ca_{i,max}$ from 189 to 199 nM).

The only study to report experimental data on the administration of ACh and Iso in human SAN tissue was carried out by Drouin (1997). However, the observed intrinsic pacemaking frequency was not coherent with clinical observations (30 beats min^{-1} *in vitro vs.* 70–112 beats min^{-1} *in situ*); it is therefore most probable that the effects of ACh and Iso were exacerbated. Furthermore, ACh and Iso targets are not electrophysiologically characterized in humans, and so we used experimental data from rabbit SAN. Thus, our simulations of ACh and Iso effects provide theoretical insights about the mechanisms underlying autonomic modulation that may require updates with respect to future data that become available from human tissue.

The administration of 10 nM ACh led to a reduction of the pacemaking rate as a result of the activation of $I_{K,ACh}$ together with changes to I_f, SR uptake and I_{CaL}. The ACh-induced reduction of I_f and activation of $I_{K,ACh}$ appeared to be the major determinants of rate slowdown.

The overall pacing rate acceleration as a result of the administration of 1 μM Iso was the result of a balance between opposing contributors. An assessment of the role of each of the five targets (I_f, I_{NaK}, I_{CaL}, I_{Ks} and SR uptake) showed that both I_f and I_{CaL} changes led to a faster beating rate. However, the underlying mechanisms were different: I_f worked on the early phase of DD, modifying DDR_{100} (also shown in I_f modulation caused by shifts in voltage dependence), whereas I_{CaL} exerted its effect during late DD. I_{NaK} showed an enhanced activity with Iso that decreased DDR and therefore counteracted the overall pacing rate acceleration.

An important test of the validity of the model was its ability to reproduce the clinical range of human heart rate. Our model was able to provide stable automaticity at ~40 beats min^{-1} upon administration of 25 nM of ACh, whereas the maximum rate (180 beats min^{-1}) was obtained by enhancing the effects of Iso on its target parameters.

The overall message from model-based simulations of autonomic modulation of pacemaking is that I_f plays an important role in rate regulation, as in rabbit. However, at least one other current ($I_{K,ACh}$ for ACh and I_{CaL} for Iso administration) needs to be modulated to achieve pacemaking rate regulation in the full physiological range.

Limitations and future developments

One evident limitation of the present study is that there are insufficient experimental data available on human SAN electrophysiology to fully constrain the parameters of the model. It is therefore possible that some non-human-specific aspects of the parent (rabbit) model are still present. This could be the case for some aspects of the calcium handling, which could underlie the very high frequency of spontaneous calcium oscillations. The present model thus only represents one step forward in the quantitative description of human SAN electrophysiology. Further experiments carried out on human adult SAN cells, or perhaps even on human induced pluripotent stem

cell-derived cardiomyocytes, will challenge the current model, providing confirmation and/or clarifying any changes that need to be made.

Specific limitations of the model include: the lack of intracellular sodium dynamics, the stop of pacemaking beating when $[Ca^{2+}]_o$ is set to a physiological *in vivo* value (1.15 mM; Severi *et al.* 2009) and the lack of a detailed description of local calcium releases.

Conclusions

In the present study, we present a human sinus node AP model based on electrophysiological data. The model is able to reproduce the experimentally observed AP morphology, calcium transient and CL prolongation upon I_f block by 2 mM Cs^+, as well as the effects of mutations responsible for cardiac ion channelopathies associated with sinus node dysfunction.

In addition to contributing to a better understanding of the events that occur on the cellular scale, the model could be a useful tool in the design of future experiments and the study (at a preliminary stage) of the effects of drugs that aim to modulate heart rate.

Appendix 1

Model parameters and equations

Cell compartments.

$C = 57\ pF$:	cell capacitance
$L_{cell} = 67\ \mu m$:	cell length
$L_{sub} = 0.02\ \mu m$:	distance between jSR and surface membrane (submembrane space)
$R_{cell} = 3.9\ \mu m$:	cell radius
$V_{i_{part}} = 0.46$:	part of cell volume occupied with myoplasm
$V_{jsr_{part}} = 0.0012$:	part of cell volume occupied by junctional SR
$V_{nsr_{part}} = 0.0116$:	part of cell volume occupied by network SR
$V_{cell} = \pi \cdot R_{cell}{}^2 \cdot L_{cell}$:	cell volume
$V_{sub} = 2 \cdot \pi \cdot L_{sub} \cdot (R_{cell} - \frac{L_{sub}}{2}) \cdot L_{cell}$:	submembrane space volume
$V_i = V_{i_{part}} \cdot V_{cell} - V_{sub}$:	myoplasmic volume
$V_{jsr} = V_{jsr_{part}} \cdot V_{cell}$:	volume of junctional SR (Ca^{2+} release store)
$V_{nsr} = V_{nsr_{part}} \cdot V_{cell}$:	volume of network SR (Ca^{2+} release store)

Fixed ion concentrations, mM.

$Cao = 1.8$:	extracellular Ca^{2+} concentration
$Ki = 140$:	intracellular K^+ concentration
$Ko = 5.4$:	extracellular K^+ concentration
$Nao = 140$:	extracellular Na^+ concentration
$Na_i = 5.0$:	intracellular Na^+ concentration
$Mgi = 2.5$:	intracellular Mg^{2+} concentration

Variable ion concentrations, mM.

Cai:	intracellular Ca^{2+} concentration
Ca_{jsr}:	Ca^{2+} concentration in the junctional SR
Ca_{nsr}:	Ca^{2+} concentration in the network SR
Ca_{sub}:	subsarcolemmal Ca^{2+} concentration

Ionic values.

$F = 96485\ \frac{C}{mol}$:	Faraday constant
$R = 8314.472\ \frac{J}{(kmol\ K)}$:	universal gas constant
$T = 310\ K$:	absolute temperature for 37°C
$RTonF = \frac{R \cdot T}{F} = 26.72655\ mV$	
$E_{Na} = RTonF \cdot \ln \frac{Nao}{Nai}$	reversal potential for Na^+
$E_{mh} = RTonF \cdot \ln \frac{Nao + 0.12 \cdot Ko}{Nai + 0.12 \cdot Ki}$	reversal potential for fast Na^+ channel
$E_K = RTonF \cdot \ln \frac{Ko}{Ki}$	reversal potential for K^+
$E_{Ks} = RTonF \cdot \ln \frac{Ko + 0.12 \cdot Nao}{Ki + 0.12 \cdot Nai}$	reversal potential for slow rectifier K^+ channel
$E_{Ca} = 0.5 \cdot RTonF \cdot \ln \frac{Cao}{Ca_{sub}}$	reversal potential for Ca^{2+}

Sarcolemmal ion currents and their conductances.

I_f:	hyperpolarization-activated current ($g_{fNa} = 0.00268\ \mu S$, $g_{fK} = 0.00159\ \mu S$)
I_{CaL}:	L-type Ca^{2+} current ($P_{CaL} = 0.4578\ \frac{nA}{mM}$)
I_{CaT}:	T-type Ca^{2+} current ($P_{CaT} = 0.04132\ \frac{nA}{mM}$)
I_{Kr}:	delayed rectifier K^+ current, rapid component ($g_{Kr} = 0.00424\ \mu S$)
I_{Ks}:	delayed rectifier K^+ current, slow component ($g_{Ks} = 0.00065\ \mu S$)
$I_{K,ACh}$:	ACh-activated K^+ current ($g_{K,ACh} = 0.00345\ \mu S$)
I_{to}:	transient outward K^+ current ($g_{to} = 3.5 \cdot 10^{-3}\ \mu S$)
I_{Na}:	fast Na^+ current ($g_{Na} = 0.0223\ \mu S$)
I_{NaK}:	Na^+/K^+ pump current ($I_{NaK,max} = 0.08105$ nA)
I_{NaCa}:	Na^+/Ca^{2+} exchanger current ($K_{NaCa} = 3.343$ nA)
I_{Kur}:	delayed rectifier K^+ current, ultrarapid component ($g_{Kur} = 1.539 \cdot 10^{-4} \mu S$)

Modulation of sarcolemmal ion currents by ions.

$Km_{fCa} = 0.000338$ mM:	dissociation constant of Ca^{2+}-dependent I_{CaL} inactivation
$Km_{Kp} = 1.4$ mM:	half-maximal K_o for I_{NaK}
$Km_{Nap} = 14$ mM:	half-maximal Na_i for I_{NaK}
$\alpha_{fCa} = 0.0075\ s^{-1}$:	Ca^{2+} dissociation rate constant for I_{CaL}

Na^+/Ca^{2+} exchanger (NaCa) function.

$K1ni = 395.3$ mM:	intracellular Na^+ binding to first site on NaCa
$K1no = 1628$ mM:	extracellular Na^+ binding to first site on NaCa
$K2ni = 2.289$ mM:	intracellular Na^+ binding to second site on NaCa
$K2no = 561.4$ mM:	extracellular Na^+ binding to second site on NaCa
$K3ni = 26.44$ mM:	intracellular Na^+ binding to third site on NaCa
$K3no = 4.663$ mM:	extracellular Na^+ binding to third site on NaCa
$Kci = 0.0207$ mM:	intracellular Ca^{2+} binding to NaCa transporter
$Kcni = 26.44$ mM:	intracellular Na^+ and Ca^{2+} simultaneous binding to NaCa
$Kco = 3.663$ mM:	extracellular Ca^{2+} binding to NaCa transporter
$Qci = 0.1369$:	intracellular Ca^{2+} occlusion reaction of NaCa
$Qco = 0$:	extracellular Ca^{2+} occlusion reaction of NaCa
$Qn = 0.4315$:	Na^+ occlusion reaction of NaCa

Ca^{2+} diffusion.

$\tau_{dif_{Ca}} = 5.469 \cdot 10^{-5}$ s:	time constant of Ca^{2+} diffusion from the subsarcolemmal space to the myoplasm
$\tau_{tr} = 0.04$ s:	time constant of Ca^{2+} transfer from the network to junctional SR

SERCA pump.

$K_{up} = 286$ nM:	half-maximal Ca_i for Ca^{2+} uptake into the network SR
$P_{up} = 5 \frac{mM}{s}$:	rate constant for Ca^{2+} uptake by SERCA pump into the network SR
$slope_{up} = 50$ nM:	slope factor for Ca^{2+} uptake by SERCA pump into the network SR

RyR function.

$kiCa = 500 \frac{1}{mM\ s}$:	RyR Ca-dependent inactivation rate
$kim = 5\ s^{-1}$:	RyR repriming rate
$koCa = 10000 \frac{1}{mM^2\ s}$:	RyR Ca-activation rate
$kom = 660\ s^{-1}$:	RyR deactivation rate
$ks = 1.48 \cdot 10^8\ s^{-1}$:	Ca^{2+} diffusion rate
$EC50_{SR} = 0.45$ mM:	EC50 for Ca_{jsr}-dependent activation of SR Ca release
$HSR = 2.5$:	Hill coefficient for Ca_{jsr}-dependent activation of SR calcium release
$MaxSR = 15$:	parameter for maximum SR calcium release
$MinSR = 1$:	parameter for minimum SR calcium release

Ca^{2+} and Mg^{2+} buffering.

$CM_{tot} = 0.045$ mM:	total calmodulin concentration
$CQ_{tot} = 10$ mM:	total calsequestrin concentration
$TC_{tot} = 0.031$ mM:	total concentration of the troponin-Ca^{2+} site
$TMC_{tot} = 0.062$ mM:	total concentration of the troponin-Mg^{2+} site
$kb_{CM} = 542\ s^{-1}$:	Ca^{2+} dissociation constant for calmodulin
$kb_{CQ} = 445\ s^{-1}$:	Ca^{2+} dissociation constant for calsequestrin
$kb_{TC} = 446\ s^{-1}$:	Ca^{2+} dissociation constant for the troponin-Ca^{2+} site
$kb_{TMC} = 7.51\ s^{-1}$:	Ca^{2+} dissociation constant for the troponin-Mg^{2+} site
$kb_{TMM} = 751\ s^{-1}$:	Mg^{2+} dissociation constant for the troponin-Mg^{2+} site
$kf_{CM} = 1.642 \cdot 10^6 \frac{1}{mM\ s}$:	Ca^{2+} association constant for calmodulin
$kf_{CQ} = 175.4 \frac{1}{mM\ s}$:	Ca^{2+} association constant for calsequestrin
$kf_{TC} = 88800 \frac{1}{mM\ s}$:	Ca^{2+} association constant for the troponin-Ca^{2+} site
$kf_{TMC} = 227700 \frac{1}{mM\ s}$:	Ca^{2+} association constant for the troponin-Mg^{2+} site
$kf_{TMM} = 2277 \frac{1}{mM\ s}$:	Mg^{2+} association constant for the troponin-Mg^{2+} site

Model equations

Membrane potential.

$$\frac{dV}{dtime} = \frac{-I_{tot}}{C}$$

$$I_{tot} = I_f + I_{CaL} + I_{CaT} + I_{Kr} + I_{Ks} + I_{K,ACh} + I_{to} + I_{Na} + I_{NaK} + I_{NaCa} + I_{Kur}$$

Ion currents.

x_∞:	steady-state for gating variable x
τ_x:	time constant for gating variable x [s]
α_x and β_x:	opening and closing rates for channel gate x [s^{-1}]

Hyperpolarization-activated, 'funny current' (I_f).

$$I_f = I_{fNa} + I_{fK}$$

$$I_{fNa} = y \cdot g_{f_{Na}} \cdot (V - E_{Na})$$

$$I_{fK} = y \cdot g_{f_K} \cdot (V - E_K)$$

$$y_\infty = \begin{cases} 0.01329 + \frac{0.99921}{1+e^{\frac{V+97.134}{8.1752}}}, & \text{if } V < -80 \\ 0.0002501 \cdot e^{\frac{-V}{12.861}}, & \text{otherwise} \end{cases}$$

$$\tau_y = \frac{1}{\frac{0.36\cdot(V+148.8)}{e^{0.066\cdot(V+148.8)}-1} + \frac{0.1\cdot(V+87.3)}{1-e^{-0.2\cdot(V+87.3)}}} - 0.054$$

$$\frac{dy}{dtime} = \frac{y_\infty - y}{\tau_y}$$

L-type Ca^{2+} current (I_{CaL}).

$$I_{CaL} = I_{siCa} + I_{siK} + I_{siNa}$$

$$I_{siCa} = \frac{2\cdot P_{CaL}\cdot V}{RTonF\cdot\left(1-e^{\frac{-2V}{RTonF}}\right)}\cdot\left(Ca_{sub} - Cao\cdot e^{\frac{-2V}{RTonF}}\right)\cdot dL\cdot fL\cdot fCa$$

$$I_{siK} = \frac{0.000365\cdot P_{CaL}\cdot V}{RTonF\cdot\left(1-e^{\frac{-V}{RTonF}}\right)}\cdot\left(Ki - Ko\cdot e^{\frac{-V}{RTonF}}\right)\cdot dL\cdot fL\cdot fCa$$

$$I_{siNa} = \frac{0.0000185\cdot P_{CaL}\cdot V}{RTonF\cdot\left(1-e^{\frac{-V}{RTonF}}\right)}\cdot\left(Nai - Nao\cdot e^{\frac{-V}{RTonF}}\right)\cdot dL\cdot fL\cdot fCa$$

$$dL_\infty = \frac{1}{1+e^{\frac{-(V+16.45)}{4.337}}}$$

$$\alpha_{dL} = \frac{-0.02839\cdot(V+41.8)}{e^{\frac{-(V+41.8)}{2.5}}-1} - \frac{0.0849\cdot(V+6.8)}{e^{\frac{-(V+6.8)}{4.8}}-1}$$

$$\beta_{dL} = \frac{0.01143\cdot(V+1.8)}{e^{\frac{V+1.8}{2.5}}-1}$$

$$\tau_{dL} = \frac{0.001}{\alpha_{dL}+\beta_{dL}}$$

$$\frac{ddL}{dtime} = \frac{dL_\infty - dL}{\tau_{dL}}$$

$$fCa_\infty = \frac{Km_{fCa}}{Km_{fCa}+Ca_{sub}}$$

$$\tau_{fCa} = \frac{0.001\cdot fCa_\infty}{\alpha_{fCa}}$$

$$\frac{dfCa}{dtime} = \frac{fCa_\infty - fCa}{\tau_{fCa}}$$

$$fL_\infty = \frac{1}{1+e^{\frac{V+37.4}{5.3}}}$$

$$\tau_{fL} = 0.001\cdot\left(44.3 + 230\cdot e^{-\left(\frac{V+36}{10}\right)^2}\right)$$

$$\frac{dfL}{dtime} = \frac{fL_\infty - fL}{\tau_{fL}}$$

T-type Ca^{2+} current (I_{CaT}).

$$I_{CaT} = \frac{2\cdot P_{CaT}\cdot V}{RTonF\cdot\left(1-e^{\frac{-2\cdot V}{RTonF}}\right)}\cdot\left(Ca_{sub} - Cao\cdot e^{\frac{-2\cdot V}{RTonF}}\right)\cdot dT\cdot fT$$

$$dT_\infty = \frac{1}{1+e^{\frac{-(V+38.3)}{5.5}}}$$

$$\tau_{dT} = \frac{0.001}{1.068\cdot e^{\frac{V+38.3}{30}} + 1.068\cdot e^{\frac{-(V+38.3)}{30}}}$$

$$\frac{ddT}{dtime} = \frac{dT_\infty - dT}{\tau_{dT}}$$

$$fT_\infty = \frac{1}{1+e^{\frac{V+58.7}{3.8}}}$$

$$\tau_{fT} = \frac{1}{16.67\cdot e^{\frac{-(V+75)}{83.3}} + 16.67\cdot e^{\frac{V+75}{15.38}}}$$

$$\frac{dfT}{dtime} = \frac{fT_\infty - fT}{\tau_{fT}}$$

Rapidly activating delayed rectifier K^+ current (I_{Kr}).

$$I_{Kr} = g_{Kr}\cdot(V - E_K)\cdot(0.9\cdot paF + 0.1\cdot paS)\cdot piy$$

$$paF_\infty = paS_\infty = pa_\infty = \frac{1}{1+e^{\frac{-(V+10.0144)}{7.6607}}}$$

$$\tau_{paS} = \frac{0.84655354}{4.2\cdot e^{\frac{V}{17}} + 0.15\cdot e^{\frac{-V}{21.6}}}$$

$$\tau_{paF} = \frac{1}{30\cdot e^{\frac{V}{10}} + e^{\frac{-V}{12}}}$$

$$\frac{dpaS}{dtime} = \frac{pa_\infty - paS}{\tau_{paS}}$$

$$\frac{dpaF}{dtime} = \frac{pa_\infty - paF}{\tau_{paF}}$$

$$\tau_{piy} = \frac{1}{100\cdot e^{\frac{-V}{54.645}} + 656\cdot e^{\frac{V}{106.157}}}$$

$$piy_\infty = \frac{1}{1+e^{\frac{V+28.6}{17.1}}}$$

$$\frac{dpiy}{dtime} = \frac{piy_\infty - piy}{\tau_{piy}}$$

Slowly activating delayed rectifier K⁺ current (I_{Ks}).

$$I_{\mathrm{Ks}} = g_{\mathrm{Ks}} \cdot (V - E_{\mathrm{Ks}}) \cdot n^2$$

$$n_\infty = \sqrt{\frac{1}{1 + e^{\frac{-(V+0.6383)}{10.7071}}}}$$

$$\tau_{\mathrm{n}} = \frac{1}{\alpha_{\mathrm{n}} + \beta_{\mathrm{n}}}$$

$$\alpha_{\mathrm{n}} = \frac{28}{1 + e^{\frac{-(V-40)}{3}}}$$

$$\beta_{\mathrm{n}} = 1 \cdot e^{\frac{-(V-5)}{25}}$$

$$\frac{\mathrm{d}n}{\mathrm{d}time} = \frac{n_\infty - n}{\tau_{\mathrm{n}}}$$

ACh-activated K⁺ current ($I_{K,ACh}$).

$$I_{\mathrm{K,ACh}} = \begin{cases} g_{\mathrm{K,ACh}} \cdot (V - E_{\mathrm{K}}) \cdot \left(1 + e^{\frac{V+20}{20}}\right) \cdot a, & \text{if } ACh > 0 \\ 0, & \text{otherwise} \end{cases}$$

$$\alpha_{\mathrm{a}} = \frac{3.5988 - 0.025641}{1 + \frac{0.0000012155}{(ACh)^{1.6951}}} + 0.025641$$

$$\beta_{\mathrm{a}} = 10 \cdot e^{0.0133 \cdot (V+40)}$$

$$a_\infty = \frac{\alpha_{\mathrm{a}}}{\alpha_{\mathrm{a}} + \beta_{\mathrm{a}}}$$

$$\tau_{\mathrm{a}} = \frac{1}{\alpha_{\mathrm{a}} + \beta_{\mathrm{a}}}$$

$$\frac{\mathrm{d}a}{\mathrm{d}time} = \frac{a_\infty - a}{\tau_{\mathrm{a}}}$$

Transient outward K⁺ current (I_{to}).

$$I_{\mathrm{to}} = g_{\mathrm{to}} \cdot (V - E_{\mathrm{K}}) \cdot q \cdot r$$

$$q_\infty = \frac{1}{1 + e^{\frac{V+49}{13}}}$$

$$\tau_{\mathrm{q}} = 0.001 \cdot 0.6 \cdot \left(\frac{65.17}{0.57 \cdot e^{-0.08 \cdot (V+44)} + 0.065 \cdot e^{0.1 \cdot (V+45.93)}} + 10.1\right)$$

$$\frac{\mathrm{d}q}{\mathrm{d}time} = \frac{q_\infty - q}{\tau_{\mathrm{q}}}$$

$$r_\infty = \frac{1}{1 + e^{\frac{-(V-19.3)}{15}}}$$

$$\tau_{\mathrm{r}} = 0.001 \cdot 0.66 \cdot 1.4 \cdot \left(\frac{15.59}{1.037 \cdot e^{0.09 \cdot (V+30.61)} + 0.369 \cdot e^{-0.12 \cdot (V+23.84)}} + 2.98\right)$$

$$\frac{\mathrm{d}r}{\mathrm{d}time} = \frac{r_\infty - r}{\tau_{\mathrm{r}}}$$

Na⁺ current (I_{Na}).

$$I_{\mathrm{Na}} = g_{\mathrm{Na}} \cdot m^3 \cdot h \cdot (V - E_{\mathrm{mh}})$$

$$m_\infty = \frac{1}{1 + e^{\frac{-(V+42.0504)}{8.3106}}}$$

$$E0_{\mathrm{m}} = V + 41$$

$$\alpha_{\mathrm{m}} = \frac{200 \cdot E0_{\mathrm{m}}}{1 - e^{-0.1 \cdot E0_{\mathrm{m}}}}$$

$$\beta_{\mathrm{m}} = 8000 \cdot e^{-0.056 \cdot (V+66)}$$

$$\tau_{\mathrm{m}} = \frac{1}{\alpha_{\mathrm{m}} + \beta_{\mathrm{m}}}$$

$$\frac{\mathrm{d}m}{\mathrm{d}time} = \frac{m_\infty - m}{\tau_{\mathrm{m}}}$$

$$h_\infty = \frac{1}{1 + e^{\frac{V+69.804}{4.4565}}}$$

$$\alpha_{\mathrm{h}} = 20 \cdot e^{-0.125 \cdot (V+75)}$$

$$\beta_{\mathrm{h}} = \frac{2000}{320 e^{-0.1(\mathrm{V}+75)} + 1}$$

$$\tau_{\mathrm{h}} = \frac{1}{\alpha_{\mathrm{m}} + \beta_{\mathrm{m}}}$$

$$\frac{\mathrm{d}h}{\mathrm{d}time} = \frac{h_\infty - h}{\tau_{\mathrm{h}}}$$

Na⁺/K⁺ pump current (I_{NaK}).

$$I_{\mathrm{NaK}} = I_{\mathrm{NaK,max}} \cdot \left(1 + \left(\frac{Km_{\mathrm{Kp}}}{Ko}\right)^{1.2}\right)^{-1} \cdot \left(1 + \left(\frac{Km_{\mathrm{Nap}}}{Nai}\right)^{1.3}\right)^{-1} \cdot \left(1 + e^{\frac{-(V-E_{Na}+110)}{20}}\right)^{-1}$$

Na⁺/Ca²⁺ exchanger current (I_{NaCa}).

$$I_{\mathrm{NaCa}} = \frac{K_{\mathrm{NaCa}} \cdot (x2 \cdot k21 - x1 \cdot k12)}{x1 + x2 + x3 + x4}$$

$$x1 = k41 \cdot k34 \cdot (k23 + k21) + k21 \cdot k32 \cdot (k43 + k41)$$

$$x2 = k32 \cdot k43 \cdot (k14 + k12) + k41 \cdot k12 \cdot (k34 + k32)$$

$$x3 = k14 \cdot k43 \cdot (k23 + k21) + k12 \cdot k23 \cdot (k43 + k41)$$

$$x4 = k23 \cdot k34 \cdot (k14 + k12) + k14 \cdot k21 \cdot (k34 + k32)$$

$$k43 = \frac{Nai}{K3ni + Nai}$$

$$k12 = \frac{\frac{Ca_{\text{sub}}}{Kci} \cdot e^{\frac{-Qci \cdot V}{RTonF}}}{di}$$

$$k14 = \frac{\frac{\frac{Nai}{K1ni} \cdot Nai}{K2ni} \cdot \left(1 + \frac{Nai}{K3ni}\right) \cdot e^{\frac{Qn \cdot V}{2 \cdot RTonF}}}{di}$$

$$k41 = e^{\frac{-Qn \cdot V}{2 \cdot RTonF}}$$

$$di = 1 + \frac{Ca_{\text{sub}}}{Kci} \cdot \left(1 + e^{\frac{-Qci \cdot V}{RTonF}} + \frac{Nai}{Kcni}\right) + \frac{Nai}{K1ni} \cdot \left(1 + \frac{Nai}{K2ni} \cdot \left(1 + \frac{Nai}{K3ni}\right)\right)$$

$$k34 = \frac{Nao}{K3no + Nao}$$

$$k21 = \frac{\frac{Cao}{Kco} \cdot e^{\frac{Qco \cdot V}{RTonF}}}{do}$$

$$k23 = \frac{\frac{\frac{Nao}{K1no} \cdot Nao}{K2no} \cdot \left(1 + \frac{Nao}{K3no}\right) \cdot e^{\frac{-Qn \cdot V}{2 \cdot RTonF}}}{do}$$

$$k32 = e^{\frac{Qn \cdot V}{2 \cdot RTonF}}$$

$$do = 1 + \frac{Cao}{Kco} \cdot \left(1 + e^{\frac{Qco \cdot V}{RTonF}}\right) + \frac{Nao}{K1no} \cdot \left(1 + \frac{Nao}{K2no} \cdot \left(1 + \frac{Nao}{K3no}\right)\right)$$

Ultra-rapid activating delayed rectifier K^+ current (I_{Kur}).

$$I_{\text{Kur}} = g_{\text{Kur}} \cdot r_{\text{Kur}} \cdot s_{\text{Kur}} \cdot (V - E_K)$$

$$\frac{dr_{\text{Kur}}}{dtime} = \frac{r_{\text{Kur}_\infty} - r_{\text{Kur}}}{\tau_{r_{\text{Kur}}}}$$

$$r_{\text{Kur}_\infty} = \frac{1}{1 + e^{\frac{V+6}{-8.6}}}$$

$$\tau_{r_{\text{Kur}}} = \frac{0.009}{1 + e^{\frac{V+5}{12}}} + 0.0005$$

$$\frac{ds_{\text{Kur}}}{dtime} = \frac{s_{\text{Kur}_\infty} - s_{\text{Kur}}}{\tau_{s_{\text{Kur}}}}$$

$$s_{\text{Kur}_\infty} = \frac{1}{1 + e^{\frac{V+7.5}{10}}}$$

$$\tau_{s_{\text{Kur}}} = \frac{0.59}{1 + e^{\frac{V+60}{10}}} + 3.05$$

Ca^{2+} release flux (J_{rel}) from SR via RyRs.

$$J_{\text{SRCarel}} = ks \cdot O \cdot (Ca_{\text{jsr}} - Ca_{\text{sub}})$$

$$kCaSR = MaxSR - \frac{MaxSR - MinSR}{1 + \left(\frac{EC50_{\text{SR}}}{Ca_{\text{jsr}}}\right)^{\text{HSR}}}$$

$$koSRCa = \frac{koCa}{kCaSR}$$

$$kiSRCa = kiCa \cdot kCaSR$$

$$\frac{dR}{dtime} = kim \cdot RI - kiSRCa \cdot Ca_{\text{sub}} \cdot R - \left(koSRCa \cdot Ca_{\text{sub}}^2 \cdot R - kom \cdot O\right)$$

$$\frac{dO}{dtime} = koSRCa \cdot {Ca_{\text{sub}}}^2 \cdot R - kom \cdot O - (kiSRCa \cdot Ca_{\text{sub}} \cdot O - kim \cdot I)$$

$$\frac{dI}{dtime} = kiSRCa \cdot Ca_{\text{sub}} \cdot O - kim \cdot I - \left(kom \cdot I - koSRCa \cdot Ca_{\text{sub}}^2 \cdot RI\right)$$

$$\frac{dRI}{dtime} = kom \cdot I - koSRCa \cdot {Ca_{\text{sub}}}^2 \cdot RI - (kim \cdot RI - kiSRCa \cdot Ca_{\text{sub}} \cdot R)$$

Intracellular Ca^{2+} fluxes.

$J_{Ca_{dif}}$: Ca^{2+} diffusion flux from submembrane space to myoplasm
J_{up}: Ca^{2+} uptake by the SR
J_{tr}: Ca^{2+} diffusion flux from the network to junctional SR

$$J_{\text{Ca}_{\text{dif}}} = \frac{Ca_{\text{sub}} - Cai}{\tau_{\text{dif}_{\text{Ca}}}}$$

$$J_{\text{up}} = \frac{P_{\text{up}}}{1 + e^{\frac{-(\text{Cai} - \text{K}_{\text{up}})}{slope_{\text{up}}}}}$$

$$J_{\text{tr}} = \frac{Ca_{\text{nsr}} - Ca_{\text{jsr}}}{\tau_{\text{tr}}}$$

Ca^{2+} buffering.

f_{CMi}: fractional occupancy of calmodulin by Ca^{2+} in myoplasm
f_{CMs}: fractional occupancy of calmodulin by Ca^{2+} in subspace
f_{CQ}: fractional occupancy of calsequestrin by Ca^{2+}
f_{TC}: fractional occupancy of the troponin-Ca^{2+} site by Ca^{2+}
f_{TMC}: fractional occupancy of the troponin-Mg^{2+} site by Ca^{2+}
f_{TMM}: fractional occupancy of the troponin-Mg^{2+} site by Mg^{2+}

$$\frac{\mathrm{d}f\,TC}{\mathrm{d}time} = \delta_{\mathrm{fTC}}$$

$$\delta_{\mathrm{fTC}} = kf_{\mathrm{TC}} \cdot Cai \cdot (1 - f\,TC) - kb_{\mathrm{TC}} \cdot f\,TC$$

$$\frac{\mathrm{d}f\,TMC}{\mathrm{d}time} = \delta_{\mathrm{fTMC}}$$

$$\delta_{\mathrm{fTMC}} = kf_{\mathrm{TMC}} \cdot Cai \cdot (1 - (f\,TMC + f\,TMM)) - kb_{\mathrm{TMC}} \cdot f\,TMC$$

$$\frac{\mathrm{d}f\,TMM}{\mathrm{d}time} = \delta_{\mathrm{fTMM}}$$

$$\delta_{\mathrm{fTMM}} = kf_{\mathrm{TMM}} \cdot Mgi \cdot (1 - (f\,TMC + f\,TMM)) - kb_{\mathrm{TMM}} \cdot f\,TMM$$

$$\frac{\mathrm{d}f\,CMi}{\mathrm{d}time} = \delta_{\mathrm{fCMi}}$$

$$\delta_{\mathrm{fCMi}} = kf_{\mathrm{CM}} \cdot Cai \cdot (1 - f\,CMi) - kb_{\mathrm{CM}} \cdot f\,CMi$$

$$\frac{\mathrm{d}f\,CMs}{\mathrm{d}time} = \delta_{\mathrm{fCMs}}$$

$$\delta_{\mathrm{fCMs}} = kf_{\mathrm{CM}} \cdot Ca_{\mathrm{sub}} \cdot (1 - f\,CMs) - kb_{\mathrm{CM}} \cdot f\,CMs$$

$$\frac{\mathrm{d}f\,CQ}{\mathrm{d}time} = \delta_{\mathrm{fCQ}}$$

$$\delta_{\mathrm{fCQ}} = kf_{\mathrm{CQ}} \cdot Ca_{\mathrm{jsr}} \cdot (1 - f\,CQ) - kb_{\mathrm{CQ}} \cdot f\,CQ$$

Dynamics of Ca^{2+} concentrations in cell compartments.

$$\frac{\mathrm{d}Cai}{\mathrm{d}time} = \frac{1 \cdot (J_{\mathrm{Ca_{dif}}} \cdot V_{\mathrm{sub}} - J_{\mathrm{up}} \cdot V_{\mathrm{nsr}})}{V_{\mathrm{i}}} - (CM_{\mathrm{tot}} \cdot \delta_{\mathrm{fCMi}} + TC_{tot} \cdot \delta_{\mathrm{fTC}} + TMC_{\mathrm{tot}} \cdot \delta_{\mathrm{fTMC}})$$

$$\frac{\mathrm{d}Ca_{\mathrm{sub}}}{\mathrm{d}time} = \frac{J_{\mathrm{SRCarel}} \cdot V_{\mathrm{jsr}}}{V_{\mathrm{sub}}} - \left(\frac{i_{\mathrm{siCa}} + i_{\mathrm{CaT}} - 2 \cdot i_{\mathrm{NaCa}}}{2 \cdot F \cdot V_{\mathrm{sub}}} + j_{\mathrm{Ca_{dif}}} + CM_{\mathrm{tot}} \cdot \delta_{\mathrm{fCMs}}\right)$$

$$\frac{\mathrm{d}Ca_{\mathrm{nsr}}}{\mathrm{d}time} = J_{\mathrm{up}} - \frac{J_{\mathrm{tr}} \cdot V_{\mathrm{jsr}}}{V_{\mathrm{nsr}}}$$

$$\frac{\mathrm{d}Ca_{\mathrm{jsr}}}{\mathrm{d}time} = J_{\mathrm{tr}} - (J_{\mathrm{SRCarel}} + CQ_{\mathrm{tot}} \cdot \delta_{\mathrm{fCQ}})$$

Rate modulation experiments

ACh 10 nM.

I_f:	shift of y_∞ and τ_y by −5 mV
I_{CaL}:	reduction of the maximal conductance by 3%
SERCA pump:	decrease of P_{up} by 7%
$I_{K,ACh}$:	activation

Isoprenaline 1 μM.

I_f:	shift of y_∞ and τ_y by 7.5 mV
I_{NaK}:	increase of $I_{NaK,max}$ by 20%
I_{CaL}:	increase of the maximal conductance by 23%; shift of dL_∞ and τ_{dL} by −8 mV; reduction of the slope factor k_{dL} by 27%
I_{Ks}:	increase of g_{Ks} by 20%; shift of n_∞ and τ_n by −14 mV
SERCA pump:	increase of P_{up} by 25%

Appendix 2

Parameters selected for automatic optimization

g_{Kur} =	maximal conductance of I_{Kur}
K_{NaCa} =	maximal current of NCX
K_{up} =	Ca^{2+} concentration for half-maximal activity of SERCA pump
P_{CaT} =	permeability of T-type Ca^{2+} current
P_{CaL} =	permeability of L-type Ca^{2+} current
k_{dL} =	slope factor of L-type voltage-dependent activation gate dL
V_{dL} =	half-maximal activation voltage of voltage-dependent activation gate dL
τ_{difCa} =	time constant of Ca^{2+} diffusion from the submembrane to myoplasm
k_s =	maximal rate of calcium release from RyR channels
kf_{CM} =	Ca^{2+} association constant for calmodulin

kf_{CQ} = Ca^{2+} association constant for calsequestrin
$I_{NaK,max}$ = maximal Na^+/K^+ pump current

Action potential features used to constrain model parameters

Experimental data on APA, MDP, CL, V_{max}, APD_{20}, APD_{50}, APD_{90}, DDR_{100} and CL prolongation induced by Cs^+ of single isolated human SAN cells as reported by Verkerk *et al.* (2007*b*) were used to constrain model parameters.

Data on CL prolongation induced by Cs^+ are from only one cell. We arbitrarily adopted an SEM of 10% of the experimentally observed CL prolongation.

Calcium transient features used to constrain model parameters

Experimental data on diastolic $[Ca^{2+}]$, systolic $[Ca^{2+}]$, TD_{20}, TD_{50} and TD_{90} of a single isolated human SAN cell as reported by Verkerk *et al.* (2013) were used to constrain model parameters.

Because the experimental data on the calcium transient are from only one cell, we arbitrarily set the SEM of each of the calcium transient features to 40% in our optimization procedure.

Cost function

In our optimization procedure, we minimized the overall cost function *FCost*, which was defined as:

$$FCost = \sum_{i} Cost_i$$

in which $Cost_i$ denotes the individual contribution of feature *i* to the overall cost.

$Cost_i$ is described as (Fig. A1):

$$\begin{cases} Cost_i = \frac{|Feature_{i,Exp} - Feature_{i,Sim}| - SEM_i}{SEM_i} weight_i & if \ |Feature_{i,Exp} - Feature_{i,Sim}| > SEM \\ 0 & otherwise \end{cases}$$

We set $weight_i = 2$ for MDP, CL and CL prolongation induced by Cs^+, whereas $weight_i$ was set to 1 for all other features.

Search method and stop criterion

The initial values of the selected parameters were obtained from the parent (rabbit) model and then manually tuned to achieve beating rate and action potential morphology close to the experimental human data. Such initial values were then employed to perform the above-mentioned finer automatic optimization.

The minimization of the overall cost function *FCost* was based on the Nelder–Mead simplex method (Lagarias *et al.*

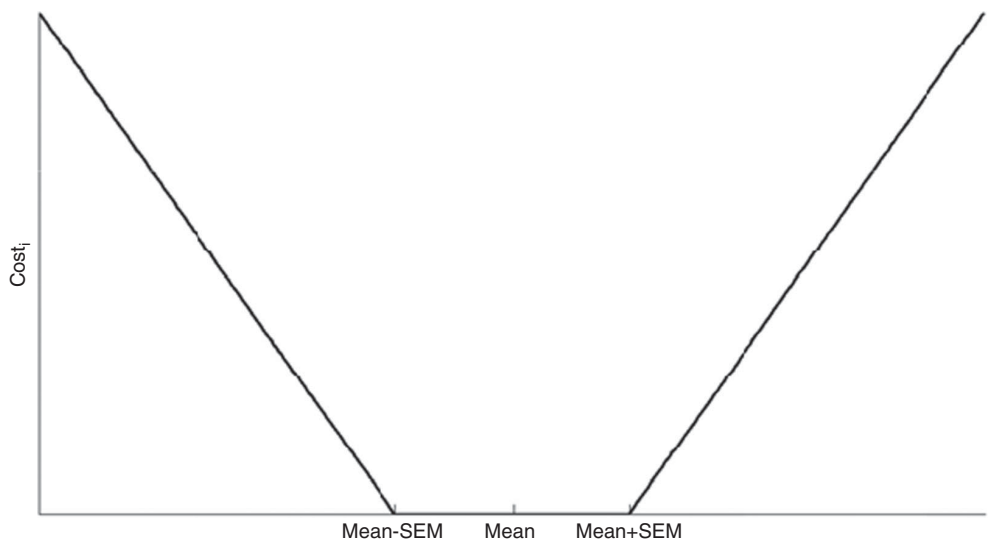

Figure A1. Cost function in optimization procedure
Contribution $Cost_i$ of feature *i* to the overall cost function (*FCost*).

Table A1. Nominal values and ranges for the optimized parameters

Parameters	Units	Nominal	Range (minimum – maximum)
g_{Kur}	μS	1.539×10^{-4}	$0.9895–1.633 \times 10^{-4}$
P_{CaT}	nA mM^{-1}	0.04132	0.04132–0.05191
P_{CaL}	nA mM^{-1}	0.4578	0.3475–0.5262
V_{dL}	mV	−16.45	−20.97 to −13.73
k_{dL}	mV	4.337	3.892–4.401
$I_{NaK,max}$	nA	0.08105	0.0623–0.1063
K_{NaCa}	nA	3.343	2.733–4.964
K_{up}	nM	286.1	204.6–356.2
k_s	s^{-1}	1.480×10^{8}	$1.460–1.847 \times 10^{8}$
τ_{difCa}	s	5.469×10^{-5}	$5.469–7.951 \times 10^{-5}$
kf_{CM}	mM s^{-1}	1.642×10^{6}	$1.164–1.839 \times 10^{6}$
kf_{CQ}	mM s^{-1}	175.4	155.2–194.6

1998). The automatic optimization procedure stopped when *FCost* converged on a local minimum.

Parameter constraining

To determine whether the parameters are well constrained we followed the approach by Sarkar and Sobie (2010). Accordingly, the extended Bayes theorem was exploited to define a range for parameters, for which a population of models is able to reproduce behaviour in agreement with experimental data. The parameter constraining is performed by increasing the number of features to satisfy: the higher the number of selected features, the lower the number of compatible parameter sets. In a similar way, we selected MDP, CL, APD_{90} and DDR_{100} from the available 13 extracted features, within the target range (i.e. mean ± SEM of experimental values) and obtained the ranges in Table A1.

The collected values show an adequately constrained range for the optimized parameters. To achieve this result, we exploited *a priori* knowledge during the optimization procedure; accordingly, we avoided non-physiological values (negative conductances or values too far from data reported in literature), assigning high scores to their cost function.

The achievement of more than one parameter set that falls into experimental ranges could attest the robustness of the model, which is able to adequately compensate for parameter changes without adopting parameter values beyond the physiological range.

References

Baruscotti M, Bucchi A, Milanesi R, Paina M, Barbuti A, Gnecchi-Ruscone T, Bianco E, Vitali-Serdoz L, Cappato R & DiFrancesco D (2017). A gain-of-function mutation in the cardiac pacemaker *HCN4* channel increasing cAMP sensitivity is associated with familial inappropriate sinus tachycardia. *Eur Heart J* **38**, 280–288.

Benhorin J, Taub R, Goldmit M, Kerem B, Kass RS, Windman I & Medina A (2000). Effects of flecainide in patients with new *SCN5A* mutation mutation-specific therapy for long-QT syndrome? *Circulation* **101**, 1698–1706.

Bezzina C, Veldkamp MW, van den Berg MP, Postma AV, Rook MB, Viersma J-W, van Langen IM, Tan-Sindhunata G, Bink-Boelkens MTE, van der Hout AH, Mannens MMAM & Wilde AAM (1999). A single Na^+ channel mutation causing both long-QT and Brugada syndromes. *Circ Res* **85**, 1206–1213.

Bogdanov KY, Vinogradova TM & Lakatta EG (2001). Sinoatrial nodal cell ryanodine receptor and Na^+-Ca^{2+} exchanger: molecular partners in pacemaker regulation. *Circ Res* **88**, 1254–1258.

Bucchi A, Baruscotti M, Robinson RB & DiFrancesco D (2007). Modulation of rate by autonomic agonists in SAN cells involves changes in diastolic depolarization and the pacemaker current. *J Mol Cell Cardiol* **43**, 39–48.

Chandler NJ, Greener ID, Tellez JO, Inada S, Musa H, Molenaar P, DiFrancesco D, Baruscotti M, Longhi R, Anderson RH, Billeter R, Sharma V, Sigg DC, Boyett MR & Dobrzynski H (2009). Molecular architecture of the human sinus node: insights into the function of the cardiac pacemaker. *Circulation* **119**, 1562–1575.

Courtemanche M, Ramirez RJ & Nattel S (1998). Ionic mechanisms underlying human atrial action potential properties: insights from a mathematical model. *Am J Physiol Heart Circ Physiol* **275**, H301–H321.

Danielsson C, Brask J, Sköld A-C, Genead R, Andersson A, Andersson U, Stockling K, Pehrson R, Grinnemo K-H, Salari S, Hellmold H, Danielsson B, Sylvén C & Elinder F (2013). Exploration of human, rat, and rabbit embryonic cardiomyocytes suggests K-channel block as a common teratogenic mechanism. *Cardiovasc Res* **97**, 23–32.

Denyer JC & Brown HF (1990). Pacemaking in rabbit isolated sino-atrial node cells during Cs^+ block of the hyperpolarization-activated current i_f. *J Physiol* **429**, 401–409.

Deschênes I, Baroudi G, Berthet M, Barde I, Chalvidan T, Denjoy I, Guicheney P & Chahine M (2000). Electrophysiological characterization of *SCN5A* mutations causing long QT (E1784K) and Brugada (R1512W and R1432G) syndromes. *Cardiovasc Res* **46**, 55–65.

DiFrancesco D (2010). The role of the funny current in pacemaker activity. *Circ Res* **106**, 434–446.

DiFrancesco D, Ferroni A, Mazzanti M & Tromba C (1986). Properties of the hyperpolarizing-activated current (i_f) in cells isolated from the rabbit sino-atrial node. *J Physiol* **377**, 61–88.

DiFrancesco D & Noble D (1985). A model of cardiac electrical activity incorporating ionic pumps and concentration changes. *Philos Trans R Soc Lond B Biol Sci* **307**, 353–398.

DiFrancesco D & Noble D (2012). The funny current has a major pacemaking role in the sinus node. *Heart Rhythm* **9**, 299–301.

Dokos S, Celler B & Lovell N (1996). Ion currents underlying sinoatrial node pacemaker activity: a new single cell mathematical model. *J Theor Biol* **181**, 245–272.

Drouin E (1997). Electrophysiologic properties of the adult human sinus node. *J Cardiovasc Electrophysiol* **8**, 254–258.

Duhme N, Schweizer PA, Thomas D, Becker R, Schröter J, Barends TRM, Schlichting I, Draguhn A, Bruehl C, Katus HA & Koenen M (2013). Altered *HCN4* channel C-linker interaction is associated with familial tachycardia–bradycardia syndrome and atrial fibrillation. *Eur Heart J* **34**, 2768–2775.

Grandi E, Pandit SV, Voigt N, Workman AJ, Dobrev D, Jalife J & Bers DM (2011). Human atrial action potential and Ca^{2+} model: sinus rhythm and chronic atrial fibrillation. *Circ Res* **109**, 1055–1066.

Henrion U, Zumhagen S, Steinke K, Strutz-Seebohm N, Stallmeyer B, Lang F, Schulze-Bahr E & Seebohm G (2012). Overlapping cardiac phenotype associated with a familial mutation in the voltage sensor of the *KCNQ1* channel. *Cell Physiol Biochem* **29**, 809–818.

Himeno Y, Sarai N, Matsuoka S & Noma A (2008). Ionic mechanisms underlying the positive chronotropy induced by β1-adrenergic stimulation in guinea pig sinoatrial node cells: a simulation study. *J Physiol Sci* **58**, 53–65.

Himeno Y, Toyoda F, Satoh H, Amano A, Cha CY, Matsuura H & Noma A (2011). Minor contribution of cytosolic Ca^{2+} transients to the pacemaker rhythm in guinea pig sinoatrial node cells. *Am J Physiol Heart Circ Physiol* **300**, H251–H261.

Kharche S, Yu J, Lei M & Zhang H (2011). A mathematical model of action potentials of mouse sinoatrial node cells with molecular bases. *Am J Physiol Heart Circ Physiol* **301**, H945–H963.

Ki C-S, Jung CL, Kim H, Baek K-H, Park SJ, On YK, Kim K-S, Noh SJ, Youm JB, Kim JS & Cho H (2013). A *KCNQ1* mutation causes age-dependant bradycardia and persistent atrial fibrillation. *Pflügers Arch – Eur J Physiol* **466**, 529–540.

Kurata Y, Hisatome I, Imanishi S & Shibamoto T (2002). Dynamical description of sinoatrial node pacemaking: improved mathematical model for primary pacemaker cell. *Am J Physiol Heart Circ Physiol* **283**, H2074–H2101.

Kyndt F, Probst V, Potet F, Demolombe S, Chevallier J-C, Baro I, Moisan J-P, Boisseau P, Schott J-J, Escande D & Marec HL (2001). Novel *SCN5A* mutation leading either to isolated cardiac conduction defect or Brugada syndrome in a large French family. *Circulation* **104**, 3081–3086.

Lagarias JC, Reeds JA, Wright MH & Wright PE (1998). Convergence properties of the Nelder-Mead simplex method in low dimensions. *SIAM J Optim* **9**, 112–147.

Laish-Farkash A, Glikson M, Brass D, Marek-Yagel D, Pras E, Dascal N, Antzelevitch C, Nof E, Reznik H, Eldar M & Luria D (2010). A novel mutation in the *HCN4* gene causes symptomatic sinus bradycardia in Moroccan Jews. *J Cardiovasc Electrophysiol* **21**, 1365–1372.

Lakatta EG (2010). A paradigm shift for the heart's pacemaker. *Heart Rhythm* **7**, 559–564.

Lakatta EG & DiFrancesco D (2009). What keeps us ticking: a funny current, a calcium clock, or both? *J Mol Cell Cardiol* **47**, 157–170.

Lakatta EG & Maltsev VA (2012). Rebuttal: What I_f the shoe doesn't fit? 'The funny current has a major pacemaking role in the sinus node'. *Heart Rhythm* **9**, 459–460.

Lakatta EG, Maltsev VA & Vinogradova TM (2010). A coupled SYSTEM of intracellular Ca^{2+} clocks and surface membrane voltage clocks controls the timekeeping mechanism of the heart's pacemaker. *Circ Res* **106**, 659–673.

Lederer WJ, Niggli E & Hadley RW (1990). Sodium-calcium exchange in excitable cells: fuzzy space. *Science* **248**, 283.

Lei M, Zhang H, Grace AA & Huang CL-H (2007). *SCN5A* and sinoatrial node pacemaker function. *Cardiovasc Res* **74**, 356–365.

Liu YM, Yu H, Li CZ, Cohen IS & Vassalle M (1998). Cesium effects on i_f and i_K in rabbit sinoatrial node myocytes: implications for SA node automaticity. *J Cardiovasc Pharmacol* **32**, 783–790.

Lyashkov AE, Juhaszova M, Dobrzynski H, Vinogradova TM, Maltsev VA, Juhasz O, Spurgeon HA, Sollott SJ & Lakatta EG (2007). Calcium cycling protein density and functional importance to automaticity of isolated sinoatrial nodal cells are independent of cell size. *Circ Res* **100**, 1723–1731.

Makita N, Behr E, Shimizu W, Horie M, Sunami A, Crotti L, Schulze-Bahr E, Fukuhara S, Mochizuki N, Makiyama T, Itoh H, Christiansen M, McKeown P, Miyamoto K, Kamakura S, Tsutsui H, Schwartz PJ, George AL & Roden DM (2008). The E1784K mutation in *SCN5A* is associated with mixed clinical phenotype of type 3 long QT syndrome. *J Clin Invest* **118**, 2219–2229.

Maleckar MM, Greenstein JL, Giles WR & Trayanova NA (2009). K^+ current changes account for the rate dependence of the action potential in the human atrial myocyte. *Am J Physiol Heart Circ Physiol* **297**, H1398–H1410.

Maltsev VA & Lakatta EG (2009). Synergism of coupled subsarcolemmal Ca^{2+} clocks and sarcolemmal voltage clocks confers robust and flexible pacemaker function in a novel pacemaker cell model. *Am J Physiol Heart Circ Physiol* **296**, H594–H615.

Maltsev VA & Lakatta EG (2010). Funny current provides a relatively modest contribution to spontaneous beating rate regulation of human and rabbit sinoatrial node cells. *J Mol Cell Cardiol* **48**, 804–806.

Mangoni ME, Traboulsie A, Leoni AL, Couette B, Marger L, Le Quang K, Kupfer E, Cohen-Solal A, Vilar J, Shin HS, Escande D, Charpentier F, Nargeot J & Lory P (2006). Bradycardia and slowing of the atrioventricular conduction in mice lacking $Ca_V3.1/\alpha_{1G}$ T-type calcium channels. *Circ Res* **98**, 1422–1430.

McAllister RE, Noble D & Tsien RW (1975). Reconstruction of the electrical activity of cardiac Purkinje fibres. *J Physiol* **251**, 1–59.

Milanesi R, Baruscotti M, Gnecchi-Ruscone T & DiFrancesco D (2006). Familial sinus bradycardia associated with a mutation in the cardiac pacemaker channel. *N Engl J Med* **354**, 151–157.

Milano A, Vermeer AMC, Lodder EM, Barc J, Verkerk AO, Postma AV, Van der Bilt IAC, Baars MJH, Van Haelst PL, Caliskan K, Hoedemaekers YM, Le Scouarnec S, Redon R, Pinto YM, Christiaans I, Wilde AA & Bezzina CR (2014). *HCN4* mutations in multiple families with bradycardia and left ventricular noncompaction cardiomyopathy. *J Am Coll Cardiol* **64**, 745–756.

Monfredi O, Maltsev VA & Lakatta EG (2013). Modern concepts concerning the origin of the heartbeat. *Physiology* **28**, 74–92.

Moss AJ, Zareba W, Benhorin J, Locati EH, Hall WJ, Robinson JL, Schwartz PJ, Towbin JA, Vincent GM, Lehmann MH, Keating MT, MacCluer JW & Timothy KW (1995). ECG T-wave patterns in genetically distinct forms of the hereditary long QT syndrome. *Circulation* **92**, 2929–2934.

Nagatomo T, Fan Z, Ye B, Tonkovich GS, January CT, Kyle JW & Makielski JC (1998). Temperature dependence of early and late currents in human cardiac wild-type and long Q-T ΔKPQ Na^+ channels. *Am J Physiol Heart Circ Physiol* **275**, H2016–H2024.

Noble D, Noble PJ & Fink M (2010). Competing oscillators in cardiac pacemaking historical background. *Circ Res* **106**, 1791–1797.

Noble D & Noble SJ (1984). A model of sino-atrial node electrical activity based on a modification of the DiFrancesco-Noble (1984) equations. *Proc R Soc Lond B Biol Sci* **222**, 295–304.

Nof E, Luria D, Brass D, Marek D, Lahat H, Reznik-Wolf H, Pras E, Dascal N, Eldar M & Glikson M (2007). Point mutation in the *HCN4* cardiac ion channel pore affecting synthesis, trafficking, and functional expression is associated with familial asymptomatic sinus bradycardia. *Circulation* **116**, 463–470.

Nygren A, Fiset C, Firek L, Clark JW, Lindblad DS, Clark RB & Giles WR (1998). Mathematical model of an adult human atrial cell: the role of K^+ currents in repolarization. *Circ Res* **82**, 63–81.

Pohl A, Wachter A, Hatam N & Leonhardt S (2016). A computational model of a human single sinoatrial node cell. *Biomed Phys Eng Express* **2**, 035006.

Rosen MR, Nargeot J & Salama G (2012). The case for the funny current and the calcium clock. *Heart Rhythm* **9**, 616–618.

Sarai N, Matsuoka S, Kuratomi S, Ono K & Noma A (2003). Role of individual ionic current systems in the SA node hypothesized by a model study. *Jpn J Physiol* **53**, 125–134.

Sarkar AX & Sobie EA (2010). Regression analysis for constraining free parameters in electrophysiological models of cardiac cells. *PLOS Comput Biol* **6**, e1000914.

Schweizer PA, Schröter J, Greiner S, Haas J, Yampolsky P, Mereles D, Buss SJ, Seyler C, Bruehl C, Draguhn A, Koenen M, Meder B, Katus HA & Thomas D (2014). The symptom complex of familial sinus node dysfunction and myocardial noncompaction is associated with mutations in the *HCN4* channel. *J Am Coll Cardiol* **64**, 757–767.

Seemann G, Höper C, Sachse FB, Dössel O, Holden AV & Zhang H (2006). Heterogeneous three-dimensional anatomical and electrophysiological model of human atria. *Philos Trans A Math Phys Eng Sci* **364**, 1465–1481.

Severi S, Corsi C & Cerbai E (2009). From in vivo plasma composition to in vitro cardiac electrophysiology and in silico virtual heart: the extracellular calcium enigma. *Philos Trans A Math Phys Eng Sci* **367**, 2203–2223.

Severi S, Fantini M, Charawi LA & DiFrancesco D (2012). An updated computational model of rabbit sinoatrial action potential to investigate the mechanisms of heart rate modulation. *J Physiol* **590**, 4483–4499.

Smits JPP, Koopmann TT, Wilders R, Veldkamp MW, Opthof T, Bhuiyan ZA, Mannens MMAM, Balser JR, Tan HL, Bezzina CR & Wilde AAM (2005). A mutation in the human cardiac sodium channel (E161K) contributes to sick sinus syndrome, conduction disease and Brugada syndrome in two families. *J Mol Cell Cardiol* **38**, 969–981.

Sobie EA (2009). Parameter sensitivity analysis in electrophysiological models using multivariable regression. *Biophys J* **96**, 1264–1274.

Thomas D, Wimmer A-B, Karle CA, Licka M, Alter M, Khalil M, Ulmer HE, Kathöfer S, Kiehn J, Katus HA, Schoels W, Koenen M & Zehelein J (2005). Dominant-negative I_{Ks} suppression by *KCNQ1*-ΔF339 potassium channels linked to Romano–Ward syndrome. *Cardiovasc Res* **67**, 487–497.

Ueda K, Nakamura K, Hayashi T, Inagaki N, Takahashi M, Arimura T, Morita H, Higashiuesato Y, Hirano Y, Yasunami M, Takishita S, Yamashina A, Ohe T, Sunamori M, Hiraoka M & Kimura A (2004). Functional characterization of a trafficking-defective *HCN4* mutation, D553N, associated with cardiac arrhythmia. *J Biol Chem* **279**, 27194–27198.

Veldkamp MW, Viswanathan PC, Bezzina C, Baartscheer A, Wilde AAM & Balser JR (2000). Two distinct congenital arrhythmias evoked by a multidysfunctional Na^+ channel. *Circ Res* **86**, e91–e97.

Veldkamp MW, Wilders R, Baartscheer A, Zegers JG, Bezzina CR & Wilde AAM (2003). Contribution of sodium channel mutations to bradycardia and sinus node dysfunction in LQT3 families. *Circ Res* **92**, 976–983.

Verkerk AO, van Borren MMGJ, Peters RJG, Broekhuis E, Lam KY, Coronel R, de Bakker JMT, Tan HL & Wilders R (2007*a*). Single cells isolated from human sinoatrial node: action potentials and numerical reconstruction of pacemaker current. *Conf Proc IEEE Eng Med Biol Soc* **2007**, 904–907.

Verkerk AO, van Borren MMGJ & Wilders R (2013). Calcium transient and sodium-calcium exchange current in human versus rabbit sinoatrial node pacemaker cells. *Sci World J* **2013**, e507872.

Verkerk AO, van Ginneken ACG & Wilders R (2009*a*). Pacemaker activity of the human sinoatrial node: role of the hyperpolarization-activated current, I_f. *Int J Cardiol* **132**, 318–336.
Verkerk AO & Wilders R (2010). Relative importance of funny current in human versus rabbit sinoatrial node. *J Mol Cell Cardiol* **48**, 799–801.
Verkerk AO & Wilders R (2015). Pacemaker activity of the human sinoatrial node: an update on the effects of mutations in *HCN4* on the hyperpolarization-activated current. *Int J Mol Sci* **16**, 3071–3094.
Verkerk AO, Wilders R, van Borren MMGJ, Peters RJG, Broekhuis E, Lam K, Coronel R, de Bakker JMT & Tan HL (2007*b*). Pacemaker current (I_f) in the human sinoatrial node. *Eur Heart J* **28**, 2472–2478.
Verkerk AO, Wilders R, van Borren MMGJ & Tan HL (2009*b*). Is sodium current present in human sinoatrial node cells? *Int J Biol Sci* **5**, 201–204.
Wehrens XHT, Abriel H, Cabo C, Benhorin J & Kass RS (2000). Arrhythmogenic mechanism of an LQT-3 mutation of the human heart Na^+ channel α-subunit: a computational analysis. *Circulation* **102**, 584–590.
Wilders R (2007). Computer modelling of the sinoatrial node. *Med Biol Eng Comput* **45**, 189–207.
Wilders R & Verkerk AO (2016). In quest of a sinoatrial cell model to assess the functional effects of mutations in the *HCN4* funny current gene. *Comput Cardiol* **43**, 833–836.
Yanagihara K, Noma A & Irisawa H (1980). Reconstruction of sino-atrial node pacemaker potential based on the voltage clamp experiments. *Jpn J Physiol* **30**, 841–857.
Yaniv Y, Lakatta EG & Maltsev VA (2015). From two competing oscillators to one coupled-clock pacemaker cell system. *Card Electrophysiol* **6**, 28.
Yaniv Y, Sirenko S, Ziman BD, Spurgeon HA, Maltsev VA & Lakatta EG (2013). New evidence for coupled clock regulation of the normal automaticity of sinoatrial nodal pacemaker cells: Bradycardic effects of ivabradine are linked to suppression of intracellular Ca^{2+} cycling. *J Mol Cell Cardiol* **62**, 80–89.
Zaza A (2016). Electrophysiology meets geometry. *Europace* **18**, 317–317.
Zaza A, Micheletti M, Brioschi A & Rocchetti M (1997). Ionic currents during sustained pacemaker activity in rabbit sino-atrial myocytes. *J Physiol* **505**, 677–688.
Zhang H, Holden AV, Kodama I, Honjo H, Lei M, Varghese T & Boyett MR (2000). Mathematical models of action potentials in the periphery and center of the rabbit sinoatrial node. *Am J Physiol Heart Circ Physiol* **279**, H397–H421.

Additional information

Competing interests

The authors declare that they have no competing interests.

Author contributions

SS was responsible for the study conception. AF and SS were responsible for the study design. AF was responsible for simulations AF, MF, RW and SS were responsible for data analysis. AF, MF and SS were responsible for data interpretation. AF, RW and SS were responsible for writing the manuscript. AF, MF, RW and SS were responsible for the final approval of the manuscript submitted for publication. All authors agree to be accountable for all aspects of the work. All persons designated as authors qualify for authorship, and all those who qualify for authorship are listed.

Funding

No funding was received for the present study.

Acknowledgements

We thank Dr Arie O. Verkerk (Department of Anatomy, Embryology and Physiology, Academic Medical Center, University of Amsterdam, Amsterdam, The Netherlands) for very useful discussions on experimental data obtained from the sinoatrial node cells.